

# Designing a Microhydraulically-driven Mini-robotic Squid

by

Kevin Dehan Meng

B.S., U.S. Air Force Academy (2014)

Submitted to the Department of Mechanical Engineering  
in partial fulfillment of the requirements for the degree of

Master of Science in Mechanical Engineering

at the

MASSACHUSETTS INSTITUTE OF TECHNOLOGY

June 2016

© 2016 Massachusetts Institute of Technology. All rights reserved.

Author.....  
Department of Mechanical Engineering  
May 20, 2016

Certified by.....  
Jakub Kedzierski  
MIT Lincoln Laboratory  
Research Advisor

Certified by.....  
Sang-Gook Kim  
Professor of Mechanical Engineering  
Thesis Supervisor

Accepted by.....  
Rohan Abeyaratne  
Chairman, Department Committee on Graduate Students

For public release. Distribution A. Approved for public release: unlimited distribution.

This material is based upon work supported by the Assistant Secretary of Defense for Research and Engineering under Air Force Contract No. FA8721-05-C-0002 and/or FA8702-15-D-0001. Any opinions, findings, conclusions or recommendations expressed in this material are those of the author(s) and do not necessarily reflect the views of the Assistant Secretary of Defense for Research and Engineering.

# **Designing a Microhydraulically-driven Mini-robotic Squid**

by

Kevin Dehan Meng

Submitted to the Department of Mechanical Engineering on May 20, 2016  
in partial fulfillment of the requirements for the degree of  
Master of Science in Mechanical Engineering

## **ABSTRACT**

The realization of a standalone microrobotic platform has thus far been elusive due to size, weight, and power constraints. Recently, a novel microhydraulic electrowetting actuator (MEA) has been developed at MIT Lincoln Laboratory, enabling powerful, efficient, and scalable actuation. The MEA's use of efficient ( $\eta > 65\%$ ), low-voltage electrowetting ( $<25$  V) and high power density favorably positions the actuator for applications in microrobotics, which includes systems on the centimeter-scale and below.

In this thesis, I present the design of a miniature robotic "squid" which features the MEA as the driving component. The system was inspired by cephalopod paralarvae, which predominantly rely on jet propulsion in their early stages of development. The squid robot can produce thrust by diaphragm pump-like operation, in either single-acting or double-acting modes. Since the actuator is a critical component, further modeling and analysis on the MEA is first presented and confirmed by experiments. After demonstrating actuator reliability, the design and fabrication of the squid are presented, from component-level considerations to system assembly procedures. High-resolution 3D printing methods are exploited to fabricate monolithic, multi-material structures and to develop passive flap check valves for gauging the pumping capability of MEA. The pump characteristics are modeled and tested, achieving flow rates of up to 1.79 mL/min. A finalized robotic squid design is predicted to swim at a velocity of 3 cm/s, which is comparable to that of young squid.

Suggestions are made for the continued development of the mini-robotic squid. It is hoped that the squid design presented herein will serve as a precursor to more advanced, standalone microrobotic systems, which may find use in medicine and defense-related applications.

Thesis Supervisor: Sang-Gook Kim  
Title: Professor of Mechanical Engineering



# Acknowledgements

Many thanks are owed to the people who have supported me throughout my journey at MIT. Without a doubt, my master's thesis and research would not have been possible without their help.

I have had an amazing opportunity to learn at MIT under the guidance of a wise advisor. Professor Kim has been overly generous in providing insightful guidance and big-picture lessons that I will certainly draw upon in the future. My lab mates Jeff, Katie, Ray, and Yu have been very helpful in discussing various topics and easing my transition to graduate school.

I have received tremendous support from MIT Lincoln Laboratory, where I have conducted the bulk of my research. My research advisor Jakub Kedzierski has been very influential in introducing me to MEMS research and modeling patience and innovation. I would like to thank my group leader, Mordechai Rothschild, and microfluidics group members, Shaun Berry, Todd Thorsen, Rafmag Cabrera, and Zach Weaver for sharing their enthusiastic support, technical knowledge, and time. At the TOIL and Packaging labs, I truly appreciate Dave Scott, John, and Mike Augeri for their willingness to help enable my efforts.

Outside of the laboratory, I have received much encouragement. I am always thankful for my family at home, as well as the family I've found through the campus Christian fellowship. Finally, I am grateful to God for bringing these wonderful friends and supporters into my life and for providing me wisdom and strength whenever I lacked.

# Contents

<b>Chapter 1</b>	<b>Introduction</b>	12
1.1	Thesis Objective and Contribution	13
1.2	Organization	13
<b>Chapter 2</b>	<b>Background</b>	15
2.1	Microrobotics	15
2.2	Actuation Technologies	16
2.3	Electrowetting	18
<b>Chapter 3</b>	<b>Microhydraulic Electrowetting Actuators</b>	21
3.1	Operation Concept	21
3.1.1	Capillary Pressure	21
3.1.2	Electrolytic Capacitors	22
3.1.3	Actuation Cycle	22
3.2	Fabrication	25
3.3	Modeling	28
3.3.1	Scaling	29
3.3.2	Dynamic Response	32
3.3.3	Optimization	35
3.4	Experimental	36
3.5	Reliability	39
<b>Chapter 4</b>	<b>Squid Design</b>	41
4.1	Inspiration	41
4.2	Propulsion Scheme	42
4.3	Actuator Configuration	43
4.4	Stacking Architecture	46
4.5	Actuator	48

4.6 Electrical Waveform .....	50
4.7 Modeling .....	52
4.8 Mantle .....	54
4.9 Gasket .....	57
4.10 Electrode Plate .....	58
4.11 Sealing.....	63
4.12 Buoy .....	63
4.13 Interconnects .....	64
4.14 Check Valve.....	65
<b>Chapter 5 Fabrication, Testing and Discussion .....</b>	<b>70</b>
5.1 Fabrication .....	70
5.2 Valve Testing .....	74
5.3 Assembly.....	81
5.4 Discussion .....	84
<b>Chapter 6 Conclusions.....</b>	<b>86</b>
6.1 Summary .....	86
6.2 Future Work .....	87
Bibliography .....	89



# List of Figures

Figure 1. Actuation Cycle [1] .....	24
Figure 2. Coated Actuator, 25 $\mu\text{m}$ D .....	27
Figure 3. Capillary Curve for 25 $\mu\text{m}$ D actuator .....	28
Figure 4. Power Density Scaling Trend [1] .....	32
Figure 5. Lambert W function [15].....	35
Figure 6. Experimental Setup .....	37
Figure 7. Reliability Testing .....	39
Figure 8. Single-Acting Arrangement.....	44
Figure 9. Double-Acting Squid Robot (back).....	46
Figure 10. Double-Acting Squid Robot (side).....	47
Figure 11. Actuator, 25 $\mu\text{m}$ D (backside) .....	49
Figure 12. Quadrature Waveforms .....	51
Figure 13. Mantle Design (multiple views) .....	56
Figure 14. Electrode plate with O-ring .....	59
Figure 15. Squid Electrical Circuit .....	60
Figure 16. Cantilever-type valve operation [21].....	66
Figure 17. 013 O-ring Gasket, glossy side (left) and matte side (right) .....	72
Figure 18. Valve test piece, 3x2x0.75 mm <sup>3</sup> cantilever .....	73
Figure 19. Flap valve performance .....	74
Figure 20. Expanded flap valve performance .....	76
Figure 21. Smaller flap performance .....	77
Figure 22. Pump test assembly design.....	79
Figure 23. Pumping using designed flap valves .....	80
Figure 24. After step 4 .....	83
Figure 25. After step 7 .....	83
Figure 26. After step 9 .....	84





# List of Tables

Table 1. Major actuator characteristics [9] [10] [11] [12] .....	17
Table 2. MEA Fabrication Process .....	25
Table 3. Cytop Dip-Coating Process .....	26
Table 4. Parts of Test Setup .....	38
Table 5. Actuator Specifications .....	48
Table 6. TangoPlus FLX930 Properties.....	67



# Chapter 1      Introduction

Recent work at MIT Lincoln Laboratory has led to the development of a novel microhydraulic actuator that uses electrowetting as its actuation principle [1]. This microhydraulic electrowetting actuator, or MEA, is able to “deliver high power at a relatively low voltage with an energy conversion efficiency of over 65%”. A highlighted application of the MEA is microrobotics, toward which actuation of a PDMS soft robotic hinge is demonstrated as well as energy harvesting. In soft robotics, a pneumatic or hydraulic displacement is used to interface with solid objects by expanding and deforming inflatable components. However, actuators that produce a hydraulic displacement need not be limited to soft robotics applications. Instead of coupling a hydraulic displacement to a deformable bladder, the displacement can be directed ejected into an ambient liquid environment.

Taking inspiration from nature’s squid, a microrobotic platform is designed to use microhydraulically-driven jet propulsion. Several jet-based underwater actuators have already been studied, such as vortex ring thrusters [2] and synthetic jet actuators [3]. While they may be viable options for larger-scale systems, their power requirements prohibit integration into robotic systems on the size of 1 cm and below. Given the MEA’s advantages and natural suitability for liquid environments, it offers unique potential to enable smaller, lighter, and more efficient microrobotic systems.

## **1.1 Thesis Objective and Contribution**

A bioinspired design for a microhydraulically-driven mini-robotic squid has been devised. The design is meant to provide the framework for smaller, more efficient microrobotic platforms by featuring the microhydraulic electrowetting actuator as the driving component, with the goal of eventually enabling highly maneuverable devices in terms of weight and power requirements.

A double-acting diaphragm pump configuration is adopted as the squid architecture. The various parts of the squid design are presented, from component-level analyses to system-level integration and testing. As a critical component, the MEA is studied further to verify its viability as a reliable actuation mechanism. A transient hydrodynamic model is used to predict actuation performance and thrust produced by the squid. For flow directionality control, flap-type passive check valves are designed and developed. Analysis and testing is performed on these valves before integration into the squid system.

Throughout the design process, the components were created with special consideration given to fabrication simplicity and interfacing. Lessons and common difficulties from novel fabrication techniques are shared. 3D-printing was selected to produce multi-material parts with complex geometries. Thus, 3D-printing is shown to be a practical method for rapidly prototyping components that can be interfaced with microfabricated actuators. As additive manufacturing technologies progress, it is expected that 3D-printing will become more widely accepted in microrobotics.

## **1.2 Organization**

The thesis presents the design of a mini-robotic squid, with topics including idea conception, theoretical modeling, component design, system assembly, and future directions for

testing. Chapter 2 provides background on the diverse field of microrobotics, with a specific focus on efficiency and power density limitations. From actuation performance trends, a case is made for the application of microhydraulic actuators to microrobotics. Since the MEA employs a relatively new actuation principle, Chapter 3 thoroughly discusses the concept of operation, scaling model, and further testing to verify reliability. Chapters 4 and 5 report the final design, fabrication, and discussion of the squid system and testing directions. Finally, Chapter 6 briefly summarizes the work and suggests future directions to enhance the performance of the microrobotic squid.

# Chapter 2      Background

## 2.1 Microrobotics

Microrobotics, also known as microbotics, refers to the field of study concerned with miniature robotic systems and subsystems, with a loosely defined size scale ranging from centimeters to microns. While the larger end of robots are built by hand, most of the smaller ones at the micron scale and below incorporate microfabrication processes.

Advances in microactuation technologies and fabrication methods, coupled with a strategic demand for lower SWaP (Size, Weight, and Power), has fueled interest in microrobotics from various stakeholders. Envisioned applications for microrobots include remote monitoring, surveillance, search and rescue, nanoassembly, medicine, and in-vivo surgery. Robotics platforms come as diverse as their possible applications, but most share a common factor: they are inspired by examples found in nature. This theme of bioinspiration is manifested in physical appearance, locomotion concepts, and swarm functionality.

The state of the art in microrobotics is arguably the RoboBee developed at Harvard, which uses flapping wings driven by piezoelectric bimorph actuators. Other significant advances include the Kilobot [4], and several novel concepts for untethered biomedical microrobots [5]. The Kilobot is powered by a coin-shaped inductive vibration motor, which produces a high frequency stick-slip motion for incremental movement. The CoCoRo project has developed intelligent aquatic swarm robotic systems for centimeter-scale, propeller-driven maneuvering [6].

Despite impressive efforts to mimic nature, the actuators driving these microrobotic systems are not as versatile as biological muscle, and come with unavoidable compromises.

While the aforementioned systems have offered valuable contributions to the field of microrobotics, they are accompanied by severe range limitations. Actuators needing high operating voltages must be tethered to a power supply, although research is being done on lightweight power electronics circuits [7]. Many biomedical microrobot concepts are activated under the influence of a local magnetic field, and Kilobots rely on inductive vibration motors which can be inefficient. Although limited range may not be prohibitive for some applications, a much wider functionality set could be opened up for small-scale autonomous systems that have the ability to operate remotely. In many cases, limited range is inherent in a robot's actuation mechanism. Therefore, not only are increased efficiency and reliability crucial for progress, but power density is also a key parameter [8]. Therefore, an ideal actuator for microrobotics would be efficient, robust, and have a high power-to-volume ratio.

## **2.2 Actuation Technologies**

At the microscale and beyond, many effects originally deemed negligible at the macroscale begin to dominate, enabling a diverse set of microactuation principles. Each actuation technology possesses its unique advantages, thereby giving each a niche application. For autonomous robotic systems designed to be remotely operated, the key performance metrics are efficiency, power density, and reliability. Efficiency reduces the energy consumption and increases range, and power density is critical for low size and weight constraints. An often unreported metric is reliability, or the ability to actuate repeatedly for long periods of time or for many actuation cycles without failure, which is essential to consistent remote operation. For



centimeter-scale locomotion, the actuator must also be able to produce high force and displacement.

The general force-displacement, power density, and efficiency characteristics of major microactuator technologies are presented in Table 1.

Table 1. Major actuator characteristics [9] [10] [11] [12]

<b>Type</b>	<b>Force</b>	<b>Displacement</b>	<b>Power Density</b>	<b>Efficiency</b>
Shape memory alloy	<i>High</i>	<i>High</i>	<i>High</i>	<i>Low</i>
Piezoelectric	<i>High</i>	<i>Low</i>	<i>High</i>	<i>High</i>
Dielectric elastomer	<i>Medium</i>	<i>High</i>	<i>High</i>	<i>High</i>
Thermo-pneumatic	<i>High</i>	<i>Medium</i>	<i>Low</i>	<i>Low</i>
Electromagnetic	<i>High</i>	<i>High</i>	<i>Low</i>	<i>Low</i>
Microhydraulic [13]	<i>Medium</i>	<i>High</i>	<i>High</i>	<i>High</i>

From the list of major actuators, the electrostatic class of actuators was shown to be highly efficient. This category includes dielectric elastomers, piezoelectrics, and microhydraulic actuators. Performance specifications for dielectric elastomers are promising, but they are known to fail frequently from hysteresis and electrical shorting. Piezoelectric actuators produce high forces but with relatively low displacements. However, displacement can easily be amplified by adding leverage to the piezoelectric film. Microhydraulic actuators have similar advantages as piezoelectrics, but they operate at lower frequencies and lower voltages. Since electrostatically-controlled microhydraulic actuators produce a volumetric displacement, the theoretical force-displacement characteristics are gathered by normalizing to the actuator area. Among the MEMS

actuators that are viable, electrostatic actuation augmented by hydraulic amplification seems well-positioned for microrobotics applications.

An overview of major microactuation technologies reveals that microhydraulic actuators are uniquely positioned for aquatic microrobotics applications. The comparative advantages of microhydraulic actuators indicate potential to not only further advance the diversity of microrobotics, but eventually enable untethered field-testable prototypes.

## 2.3 Electrowetting

The Bond number is a dimensionless parameter that gives the relative importance of gravitational forces to surface tension forces.

$$Bo = \frac{\rho g D^2}{\sigma}$$

with density  $\rho$ , gravitational acceleration  $g$ , meniscus diameter  $D$ , and surface tension  $\sigma$ . When  $Bo \ll 1$ , the effect of gravity can be neglected.

At  $Bo \ll 1$ , a small liquid droplet on a surface assumes a rounded profile governed by the surface energies of the material interfaces. The contact angle between the liquid, solid, and gas phases are consistently observed given the materials and conditions. The droplet contact angle is the result of a balance between cohesive forces within the droplet and adhesive forces at the solid-liquid interface, and can be consistently observed in controlled conditions. In static equilibrium, the contact angle of a droplet on a substrate can be predicted by a force balance applied at the three-phase contact line, known as Young's equation:

$$\gamma_{LV} \cos \theta_{SL} = \gamma_{SV} - \gamma_{SL}$$

where  $\theta_{SL}$  is the contact angle formed by the droplet on the substrate and  $\gamma_{ij}$  represents the surface energies of the different interfaces formed by the liquid (L), vapor (V), and solid (S) phases. It is possible for another liquid can be substituted for the vapor phase.

In electrowetting, an electric field is applied to modify the surface energy and contact angle of various liquids. The addition of an applied voltage between the liquid and solid decreases  $\gamma_{SL}$ , and consequently decreases the solid-liquid contact angle. The surface energy between liquid and solid phases is altered due to build-up of an electric double-layer that enhances attraction. Common uses for electrowetting include droplet manipulation, micro-pumping, and bio-analysis. First experimented upon by Gabriel Lippmann in 1875, electrowetting has been improved with significant advancements within the past few decades. While initial experiments yielded small contact angle changes due to electrolysis at low voltages, Bruno Berge later pioneered what is now called electrowetting-on-dielectric (EWOD), where a dielectric is inserted between the conductive solid and liquid phases allowing much higher voltages to be applied, leading to greater contact angle changes. Mugele presents a comprehensive overview of electrowetting in [14].

Electrowetting is described by the modified Young's equation:

$$\gamma_{SL} = \gamma_{SL}^0 - \frac{1}{2} C V^2$$

$$C_a = \frac{\epsilon_0 \epsilon_r}{t}$$

Where  $\gamma_{SL}^0$  is the original solid-liquid surface energy,  $C_a$  the areal capacitance with permittivity of free space  $\epsilon_0$ , dielectric constant  $\epsilon_r$ , and dielectric thickness  $t$ . The  $\frac{1}{2} C V^2$  term represents the capacitor energy, as electrowetting is a capacitive effect.

Increasing the voltage will progressively decrease the contact angle regardless of voltage polarity. This continues until the point of contact angle saturation, at roughly  $\theta_{SL} \approx 50^\circ$ , where increasing the voltage no longer lowers the contact angle. The exact point of saturation depends on material properties. [14] offers several theories behind contact angle saturation.

A common strategy to achieve large contact angle changes is to begin at a very high contact angle. Surfaces on which droplets are placed can be superhydrophobic, whether inherently or with the assistance of surface patterning and coating, or be immersed in an immiscible oil. Due to its low surface energy, the oil phase serves to increase the initial contact angle and also prevents evaporation of the working fluid. In limited voltage applications, electrowetting can still be effective by using thinner dielectrics and high-k dielectric materials to increase  $C_a$ .

# Chapter 3

## Microhydraulic Electrowetting Actuators

A specific type of capacitive actuator, named the microhydraulic electrowetting actuator (MEA), has been developed [1]. The MEA performance metrics are congruent with the expected advantages of microhydraulic actuators in general, mentioned in section 2.2. Since the MEA is the critical driving component of the proposed mini-robotic squid, this chapter thoroughly explains its concept of operation, fabrication, modeling, and experimentation, serving as a prelude to the main discussion of the robotic squid system design in Chapter 4.

### 3.1 Operation Concept

The key concepts of capillary pressure and electrolytic capacitors are outlined before proceeding to describe the actuation cycle. These effects play a significant role due to the small length scales involved.

#### 3.1.1 Capillary Pressure

The pressure across a curved liquid interface is given by the Young-Laplace equation:

$$P = \gamma \left( \frac{1}{R_1} + \frac{1}{R_2} \right)$$

where  $\gamma$  is surface tension, and  $R_1$  and  $R_2$  are the radii of curvature along orthogonal axes.

For a spherical interface with curvature diameter  $D$ , the pressure can be simplified to

$$P = \frac{4\gamma}{D}$$

Like a balloon, the pressure of the fluid on the inside, or concave side, of the curved interface is higher. A perfectly flat interface represents equal pressures on both sides.

### 3.1.2 Electrolytic Capacitors

In electrolytic capacitors, high surface area-to-volume ratio geometries are used to achieve larger capacitances within the same volume. Similarly, a high porosity capillary plate gives the MEA a high surface area-to-volume ratio. The MEA conductive capillary plate is coated with a hydrophobic dielectric to enable actuation with two immiscible liquids, 0.01 M NaCl solution (electrolyte) and decane (insulator), a hydrocarbon oil. The water-decane interface lies within the capillaries of the plate, whose surfaces are active, being able to change from hydrophobic to hydrophilic with an applied voltage. The MEA creates pressure by pulling water into the capillaries during the hydrophilic (voltage ON) state and pushing it out during the hydrophobic (voltage OFF) state.

### 3.1.3 Actuation Cycle

The MEAs have capillaries of diameter  $D$ , with a capillary stop at the end to prevent water from bleeding through the plate. Because capillary pressure scales as the inverse of capillary diameter  $D$ , the actuator becomes more powerful as capillary size scales downward.

Since the hydrophobic pressure acts from within the capillaries, a certain pressure  $P_{max}$  is needed to push water into the MEA in the OFF state, without an applied voltage.

$$P_{max} = \frac{4\gamma_{wo}}{D}$$

At  $25\ \mu\text{m}$   $D$ , this pressure is roughly equal to 8 kPa. In the ON state with an applied electrowetting voltage  $V_a$ , the pressure across the interface becomes

$$\Delta P = \frac{4}{D} (\gamma_{wo} - \frac{1}{2} C_a V_a^2) = P_{max} - \frac{2C_a V_a^2}{D}$$

The driving pressure  $P_s$  is then

$$P_s = P_b - \Delta P = P_b - (P_{max} - \frac{2C_a V_a^2}{D})$$

with a back pressure  $P_b$ . At  $V_a \approx 14 V$ ,  $\Delta P = 0$  is achieved when the contact angle is  $90^\circ$  and the opposing capillary pressure is nullified, allowing water to enter into the capillaries.

The positive back pressure  $P_b$  is applied from the water side to help drive the fluid into the device. For a balanced forward and backward flow, the back pressure is set to about half of  $P_{max}$  such that the forward and backward driving pressures are equal in magnitude.

$$P_b \approx \frac{P_{max}}{2}$$

Reversibility in electrowetting enables cyclic actuation. If the water phase bleeds through the capillaries to the other side, then the water-oil interface cannot return into the capillaries and pressure can no longer be controlled. To prevent bleed-through from happening, a capillary stop has been created at the end of the capillary on the oil-side. This capillary stop is a constriction in the diameter along with a locally thicker dielectric layer, which increases the local  $P_{max}$  while decreasing the effectiveness of electrowetting.

The MEA actuation cycle can be broken down into four steps, illustrated in Figure 1.

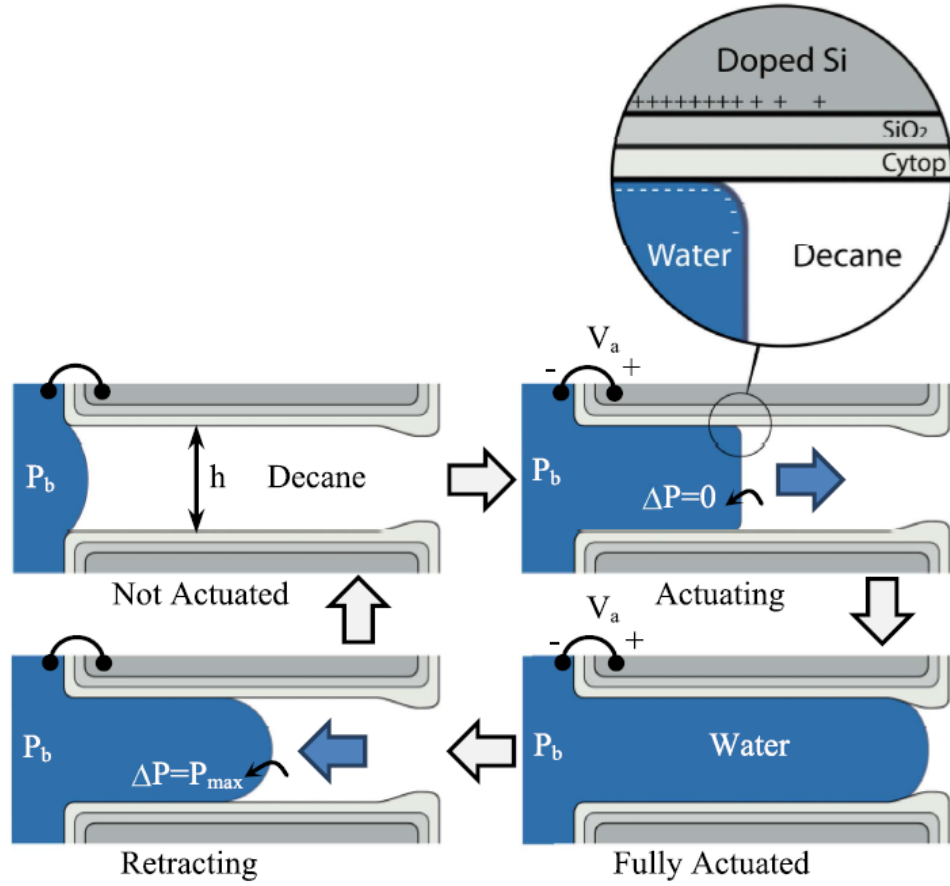


Figure 1. Actuation Cycle [1]

Step 1: Beginning at the top left of Figure 1, the MEA is initially in the OFF state, with the hydrophobic capillaries filled with decane. Water is pushed against the entrance of the capillaries under a back pressure. Without any applied voltage  $V_a = 0$ , the driving pressure  $P_s$  cannot overcome the capillary pressure at the water-oil interface.

$$P_s = P_b - \Delta P = 0$$

Step 2: Application of voltage  $V_a$  causes capillaries to become hydrophilic ( $\Delta P = 0$ ), allowing the pressurized water to push through the capillaries.

$$P_s = P_b - \Delta P = P_b$$



Step 3: At the end of the capillaries, the capillary stop impedes further meniscus movement. Allowing the water-oil meniscus to bleed through the plate would irreversibly push the electrowetting interface to the other side and disable repeated electrowetting.

Step 4: Upon removal of voltage, the capillaries become hydrophobic again which causes water to retract from the capillaries, back to the initial state in Step 1.

## 3.2 Fabrication

Three generations of MEA were fabricated having capillary diameters of 175, 25, and 12  $\mu\text{m}$ . [1] contains supplemental information detailing the microfabrication process flow. The important steps are listed here in Table 2 for quick viewing, with “F” denoting front-side processing and “B” for back-side:

Table 2. MEA Fabrication Process

Step	Description	Side	Purpose
1	Heavily doped Si wafer, 750 $\mu\text{m}$ thick		
2	Plasma deposit 2 $\mu\text{m}$ $\text{SiO}_2$ hard-mask	F	
3	Pattern capillary openings using photolithography	F	
4	Dry etch capillary openings through hard-mask	F	
5	Strip and ash photoresist in oxygen plasma and sulfuric acid/peroxide		
6	Deposit 2 $\mu\text{m}$ $\text{SiO}_2$ hard-mask	B	
7	Pattern and etch hard-mask below capillary openings to a controlled thickness	B	
8	Strip and ash photoresist		
9	Bosch plasma etch patterned region	B	Control thickness of porous area
10	Deposit another 2 $\mu\text{m}$ $\text{SiO}_2$ hard-mask	B	
11	Bosch etch capillaries into Si, stopping at back $\text{SiO}_2$ hard-mask	F	
12	Strip sidewall polymer		
13	Remove hard-masks in HF		
14	Clean wafers in sulfuric/peroxide at 120° C		

13	Smooth capillary walls in 10:3:1 acetic, nitric, and HF acid for 4 min, rinse and spin dry		Reduce hysteresis and contact line pinning
14	Grow 100 nm SiO <sub>2</sub> through thermal oxidation at 1000° C		First dielectric layer

The wafer was diced into actuator samples measuring 20 mm x 20 mm, centered on the capillary region. Next the individual samples were dip-coated in Cytop CTL-809M (Asahi Glass Co., Ltd.), an amorphous fluoropolymer, to form the second hydrophobic dielectric layer above SiO<sub>2</sub>. Cytop was diluted in Fluorinert Electronic Liquid FC-40 (3M) for a coating thickness  $t_{CT}$  of 80 nm. The Cytop concentration  $\phi$  for different plates of capillary diameter D was calculated as

$$\phi = \frac{D^2 - (D - 2t_{CT})^2}{D^2} \approx \frac{4t_{CT}}{D}$$

The dip coating process is described in Table 3.

Table 3. Cytop Dip-Coating Process

Step	Description	Purpose
1	Dip actuator into Cytop solution	
2	Tilt to drip off excess Cytop for 1 min	
3	Suspend at ambient temperature for 10 min	Dry at room temperature
4	Suspend over 110°C hotplate for 80 min	Prebake (degas)
5	Suspend in 180°C oven for 10 min	Prebake (remove solvent)
6	Clean in IPA and DI water	Final cure

Figure 2 shows a 25  $\mu$ m D actuator plate after dicing and coating. The top-right corner has been scribed to remove the dielectric, allowing room for electrical connection during testing. The etched capillary portion is cross-shaped and the multi-color hue results from the Cytop coating.

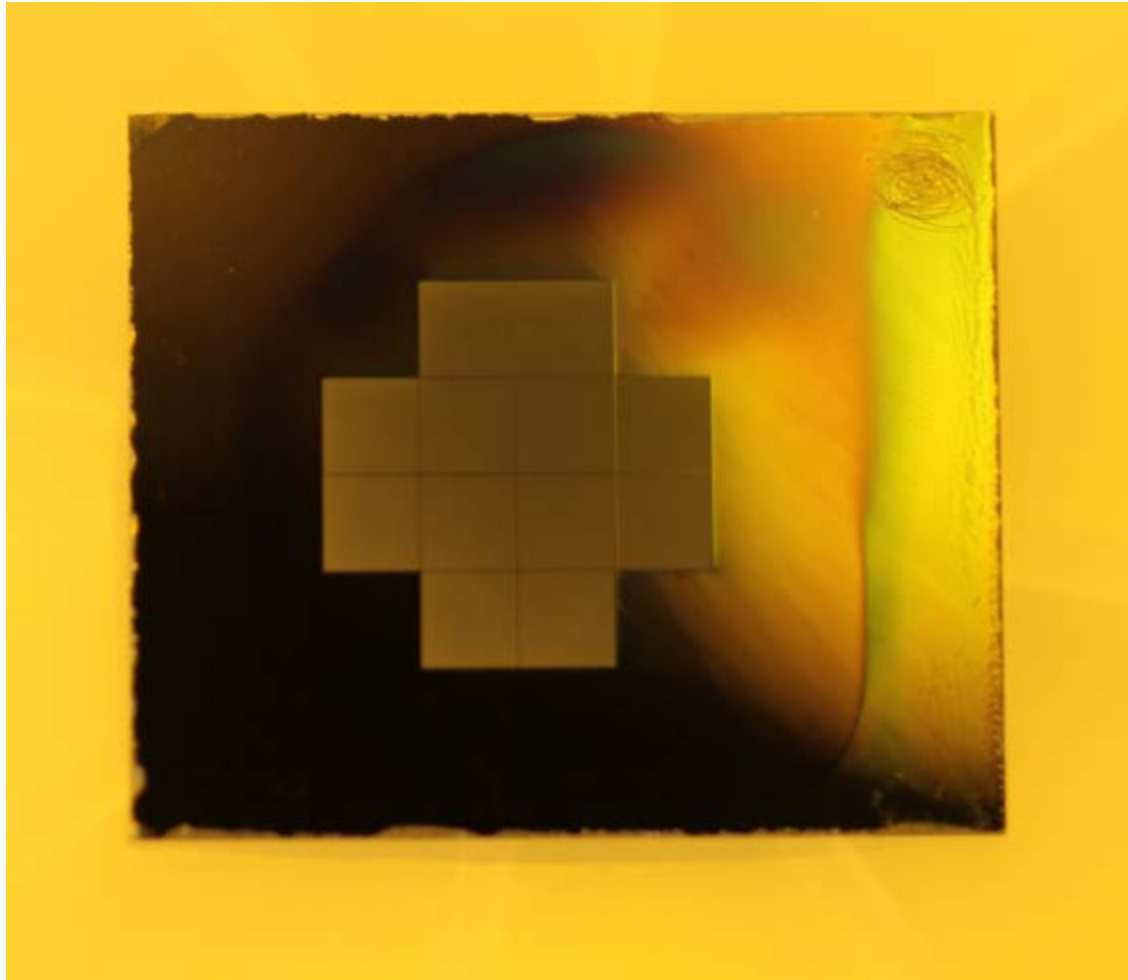


Figure 2. Coated Actuator, 25  $\mu\text{m}$  D

The capillary curve is a profile that shows the relation between back pressure and water penetration through the actuator's capillaries. The profile was acquired by steadily raising the back pressure and measuring the movement of a hydraulically linked oil-air meniscus. Upon reaching the bleed through pressure  $P_{bt}$ , the back pressure was gradually lowered back to zero. No voltage was applied to obtain the capillary curves. A representative capillary curve for 25  $\mu\text{m}$  D actuator is shown in Figure 3.

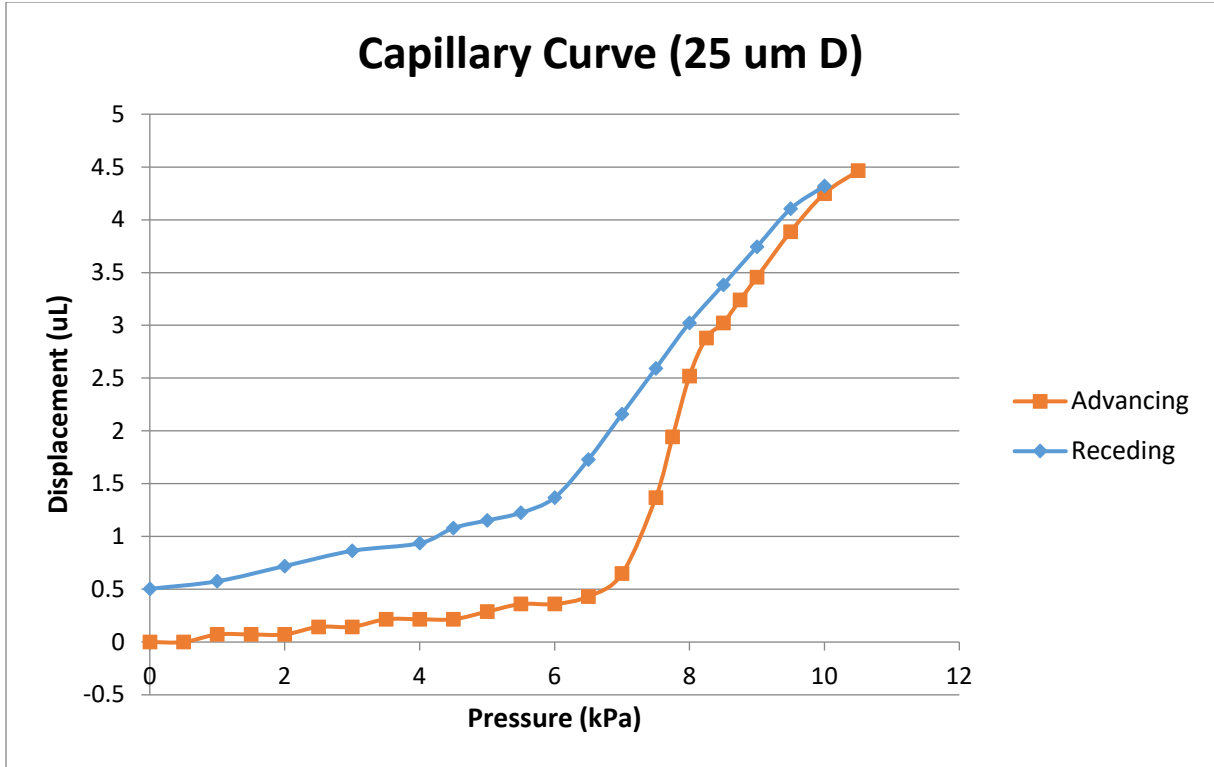


Figure 3. Capillary Curve for 25  $\mu\text{m}$  D actuator

The bottom curve is obtained by increasing pressure incrementally with an advancing meniscus, while the top curve is for decreasing pressure with a receding meniscus. The discrepancy between the two curves is due to contact angle hysteresis likely caused by surface roughness inside the capillaries. It is not until around the theoretical  $P_{max}$  at 8 kPa that a significant amount of water penetrates into the capillaries.

### 3.3 Modeling

A power density scaling relation was derived for the MEA, followed by a dynamic actuation analysis to allow more accurate performance predictions. Optimization strategies are given as guidelines for future work.

### 3.3.1 Scaling

The governing relation for hydrodynamic flow in a closed channel is given by

$$P_s = QR_s$$

where the volumetric flow rate  $Q$  is proportional to a differential pressure  $P_s$  and inversely proportional to the total hydrodynamic resistance  $R_s$ . This is analogous to Ohm's law governing electric current and voltage, with the effort variable (voltage) replaced with pressure difference and flow variable (current) replaced with volumetric flow rate.

For laminar flow ( $Re < 2100$ ) of an incompressible fluid, the Hagen-Poiseuille equation gives the hydrodynamic resistance  $R_h$  through a cylindrical pipe.

$$R_h = \frac{128\mu L}{\pi D^4}$$

Here  $\mu$  is the dynamic viscosity of the fluid,  $L$  the capillary length, and  $D$  the capillary diameter.

Because the MEA is made of  $N$  parallel cylindrical capillaries, its resistance  $R_{act}$  can be calculated as

$$R_{act} = \frac{128\mu L}{N\pi D^4}$$

To verify laminar flow, an order of magnitude estimate is performed:

$$Q = AU$$

where  $A$  is channel area and  $U$  is flow velocity. Order of magnitude values for a water-filled, 25  $\mu\text{m}$  D actuator with  $N \sim 10^4$  capillaries gives a  $Re$  on the order of

$$Re = \frac{\rho U D}{\mu} = \frac{\rho D}{\mu} \left( \frac{Q}{A} \right) = \frac{\rho D}{\mu} \left( \frac{P_s}{R_s} \right) \left( \frac{4}{N\pi D^2} \right)$$
$$Re \sim \frac{10^3 10^{-5}}{10^{-4}} \left( \frac{10^3}{10^{10}} \right) \left( \frac{4}{\pi 10^4 (10^{-5})^2} \right) \sim 10^1$$

Therefore the flow in the actuator can be assumed laminar.

In steady-state, for a volumetric flow rate of constant magnitude, the maximum actuation frequency  $f_{max}$  based on the time it takes the meniscus to traverse the capillary length  $L$  is:

$$f_{max} = \frac{Q_{ss}}{2V_{disp}} = \frac{P_s}{2R_s V_{disp}}$$

$$V_{disp} = \frac{N\pi D^2 L}{4}$$

Here  $Q_{ss}$  is the maximum flow rate and  $V_{disp}$  is the actuator volumetric displacement. Beyond the maximum frequency  $f_{max}$ , the actual displacement diminishes. This is due to hydrodynamic constraints on the meniscus speed.

Using  $f_{max}$ , the power density  $S_d$  can then be scaled as

$$S_d = \frac{E_{cyc}}{T_{cyc} V_{act}} = 2P_s f_{max} \left( \frac{V_{disp}}{V_{act}} \right)$$

with energy per cycle  $E_{cyc}$ , period  $T_{cyc}$ , and actuator volume  $V_{act}$ .

Substitution of parameters into the power density equation gives

$$S_d = \frac{\gamma_{wo}^2 D^2 F_R F_V}{8\mu L^2}$$

with resistance fraction  $F_R = R_{act}/R_s$  and volume fraction  $F_V = V_{disp}/V_{act}$ . At  $F_R = 1$ , the system is unloaded.  $F_V$  is a function of the overall porosity of the actuator, which is the capillary volume normalized by the overall actuator volume. The maximum porosity for hexagonally arranged cylindrical capillaries is 91%.

The scaling result assumes:

- Pressure fraction  $F_P = \frac{P_b}{P_{max}} = \frac{1}{2}$  or  $|P_s| = \frac{2\gamma}{D}$
- Displaced volume  $V_{disp} = \frac{N\pi L D^2}{4}$
- Entrance and exit minor losses neglected

- Dynamic viscosity of water is used  $\mu_{NaCl} = 1.16\mu_{decane}$
- Dielectric thickness  $T_d$  and roughness are negligible,  $T_d \ll D$
- Instantaneous steady-state response  $|Q_{ss}| = \text{constant}$

Given these assumptions, the result agrees with the scaling relation derived in [1].

$$S_d = \frac{\gamma_{wo}^2 D^2 F_P^2 F_R F_V}{2\mu_{eff} L (L + 4D) (D + 2T_d)^2}$$

For fixed aspect ratio capillaries, power density scales as  $1/D^2$ . This is achieved with a smaller device size  $V_{act}$  but in exchange for less displacement volume  $V_{disp}$ .

It has been demonstrated in [1] that downscaling capillary D leads to higher power density. Figure 4 plots power/strength density for actuators with three different capillary D sizes: 175, 25 and 12  $\mu\text{m}$ . The trend line from experiments is consistent with scaling predictions.

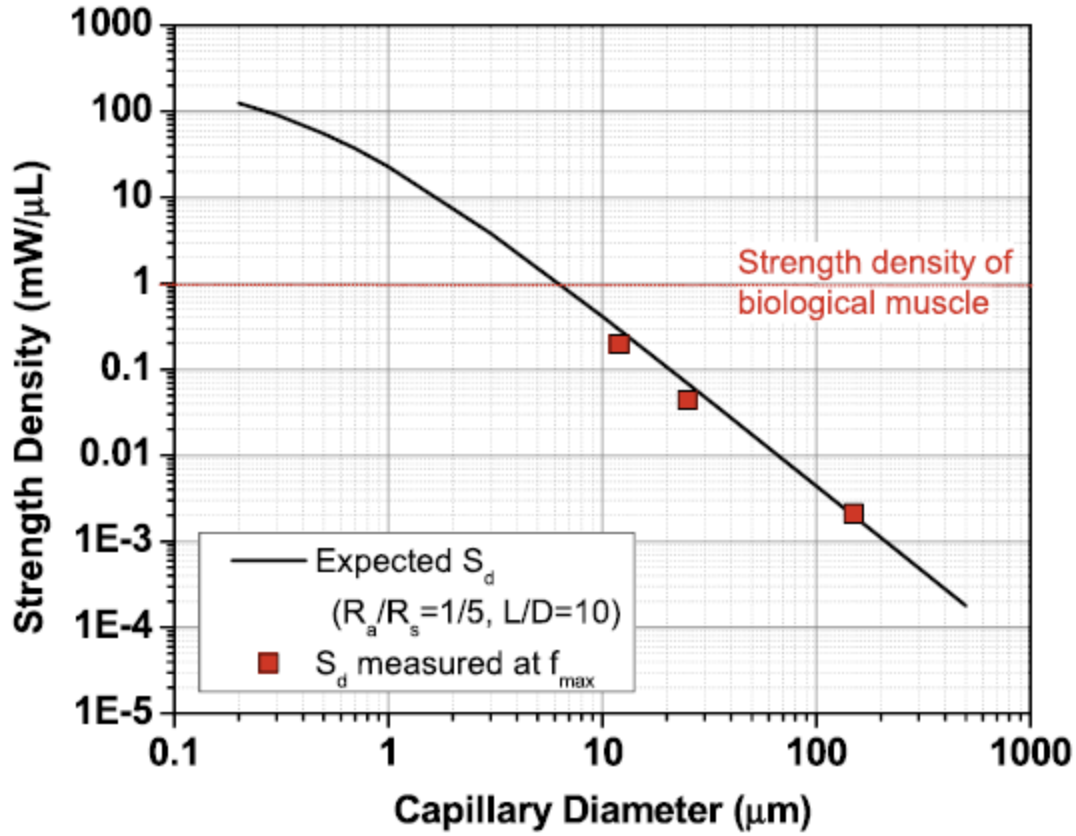


Figure 4. Power Density Scaling Trend [1]

### 3.3.2 Dynamic Response

In reality, the meniscus extension and retraction through the capillaries does not occur at a steady flow rate, but rather accelerates approaching a steady-state velocity. As capillary  $D$  is scaled down, the acceleration phase becomes a significant factor in the time it takes for full actuation to occur. For higher accuracy in modeling  $f_{max}$ , a dynamic model accounting for inertial effects was developed with the following assumptions:

- i) meniscus motion stops upon reaching the capillary ends
- ii) constant driving pressure,  $|P_s| = P_{max}/2$
- iii) ideal cylindrical capillary geometry,  $V_{disp} = NL\pi D^2/4$



An enabling factor of systems analysis across multiple domains is the parallelism found between their “effort” and “flow” variables. In this case, these similarities allow the application of electrical circuit analysis to hydraulic analysis. The hydraulic system contains an inertia and resistance, and hence can be modeled as an LR-circuit, with pressure as the *effort* variable and volumetric flow rate as the *flow* variable. When pressure is applied at time  $t = 0$ , the flow rate can be stated as

$$Q(t) = \frac{P_s}{R_s} \left( 1 - e^{-\frac{t}{\tau}} \right) = Q_{ss} (1 - e^{-\frac{t}{\tau}})$$

$$I = \frac{\rho L}{A}$$

$$R_s = \Sigma R_i = R_{act} + R_{other}$$

$$\tau = \frac{I}{R} \sim D^2$$

The hydraulic inertia  $I$  decreases as the fluidic channel expands to contain more fluid, which may seem counterintuitive. This is because pressure is a distributed areal force and a slug of fluid is easier to accelerate in a wider channel.

The system time constant  $\tau$  is a measure of the system’s reactance to pressure changes. It takes a time of roughly  $t = 3\tau$  for the system to reach steady state, during which the average flow rate is roughly two-thirds the maximum, steady-state flow rate.

$$Q(3\tau) = 0.95Q_{ss}$$

$$Q_{avg} = \frac{\int_0^{3\tau} Q(t) dt}{3\tau} = 0.683Q_{ss}$$

For an infinitely long capillary, the average flow rate approaches  $Q_{ss}$ . However, in smaller capillaries as in the MEA, the meniscus movement occurs predominantly within the acceleration phase.

$t_{fill}$  is the time it takes for the meniscus to travel across the capillaries, producing an overall displacement  $V_{disp}$  and can be solved as follows:

$$V(t) = \int_0^t Q(t)dt = \frac{P_s}{R_s} (t + e^{-\frac{t}{\tau}}\tau - \tau) \Big|_0^t = Q_{ss}[t + \tau(e^{-\frac{t}{\tau}} - 1)]$$

$$\frac{V_{disp}}{Q_{ss}} + \tau = t_{fill} + \tau e^{-\frac{t_{fill}}{\tau}}$$

Recognize that  $\frac{V_{disp}}{Q_{ss}} = \frac{1}{2f_{max}} = t_{ss}$ .

$$t_{fill} = t_{ss} + \tau + \tau W\left(-e^{-\left(\frac{t_{ss}}{\tau} + 1\right)}\right)$$

Here the Lambert W function has been used for simplification. The Lambert W function is useful for solving delayed differential equations. It is the function  $W(z)$  satisfying

$$W(z)e^{W(z)} = z$$

For real values of  $z$ ,  $W(z)$  takes on two different values from  $-\frac{1}{e} < z < 0$ . In the principal branch used in modeling, the range  $-\frac{1}{e} \leq z \leq 0$  leads to  $-1 \leq W(z) \leq 0$ . In Figure 5, the full range of  $W(z)$  is plotted.

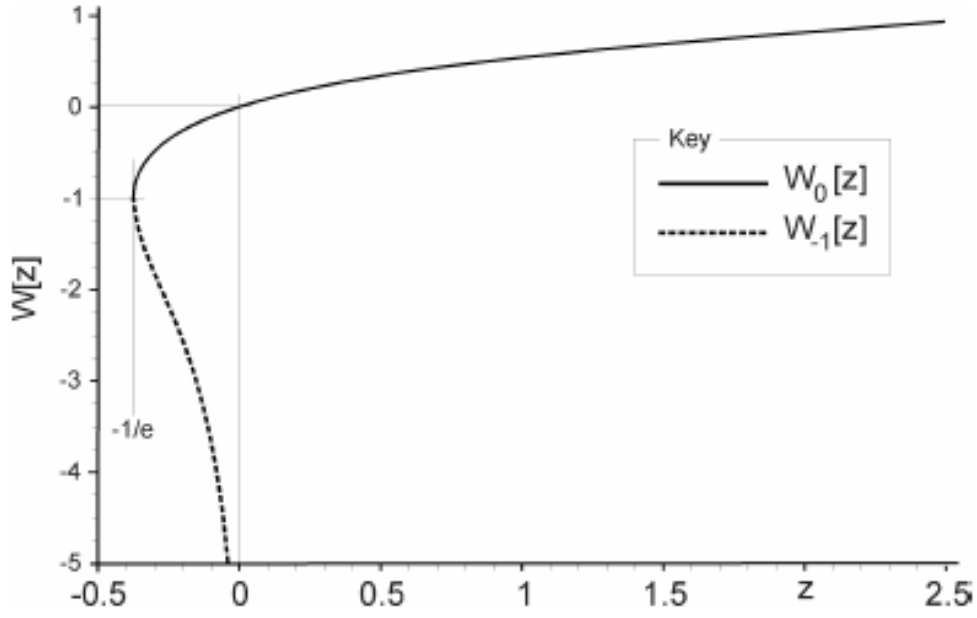


Figure 5. Lambert W function [15]

When  $\frac{t_{ss}}{\tau} \rightarrow 0$ , the result is simply  $t_{fill} = t_{ss}$ . As  $t_{ss}/\tau \rightarrow \infty$ ,  $t_{fill}$  deviates from the steady-state approximation and becomes larger, meaning acceleration plays a larger role in  $t_{fill}$  as D shrinks according to the scaling,

$$\frac{t_{ss}}{\tau} = \frac{1}{D^2}$$

Finally a more accurate  $f_{max*}$  can be predicted,

$$f_{max*} = \frac{1}{2t_{fill}} = \frac{1}{2 \left[ t_{ss} + \tau + \tau W \left( -e^{-\left(\frac{t_{ss}}{\tau} + 1\right)} \right) \right]}$$

### 3.3.3 Optimization

In general, unnecessary contributions to  $R_s$  should be eliminated. Decreasing the system hydrodynamic resistance  $R_s$  will decrease  $t_{fill}$ , regardless of whether doing so increases the

inertia  $I$ . This can be done by reducing the length and increasing the diameter of tubing, capillaries, or other components. The contribution from highly resistive segments of hydraulic circuits can also be mitigated by adding parallel paths. The equivalent resistance  $R_{AB}$  of parallel loads  $R_A$  and  $R_B$  are calculated as:

$$R_{AB} = \frac{R_A R_B}{R_A + R_B}$$

For example, the MEA has capillary diameter  $D$  on the order of microns, but the overall  $R_{act}$  is not excessive due to having  $N$  ( $O \sim 10^4$ ) parallel flow paths.

According to the maximum power transfer theorem, the greatest power is delivered to the load when the load impedance is matched with the source (actuator) impedance. For future systems, load matching should be designed for when practical.

$$R_{system} = R_{source} + R_{load}$$

$$R_{load}/R_{source} \rightarrow 1 \quad \dot{W}_{load}/\dot{W}_{max} \rightarrow 1$$

For maximum efficiency, the ratio of source to load impedance should be minimized.

$$\eta = \frac{R_{load}}{R_{load} + R_{source}} = \frac{1}{1 + R_{source}/R_{load}}$$

### 3.4 Experimental

The experimental setup is depicted in Figure 6. The actuator plate is clamped inside a metal test assembly. On the oil side, the assembly is attached to a measurement tube the observe decane-air meniscus movement, which indicates volumetric displacement. At the top of the assembly is a junction linking the actuator to tubing that leads to a manometer. The manometer is the source of back pressure to the actuator, but it can be a significant contributor to resistance due to its tubing length. However, an accumulator is connected in parallel to the manometer to

provide a pressure source closer to the actuator. A hydraulic accumulator is a device that uses compressed gas or a spring to accumulate potential energy, and is commonly used to store pressurized fluid. It can be thought of as a hydraulic capacitor that can quickly adopt the pressure set by the manometer. According to the ideal gas law, as long as  $V_{disp}$  does not cause the air within the accumulator to undergo large changes, the accumulator can supply a near-constant pressure and can even replace the manometer after its pressure is set.

$$P_{accum} = \frac{mRT}{V}$$

$$P_{accum}V_{air} = constant$$

The accumulator used here does not supply a large pressure head due to height change, so most of the pressurization comes from the compressed air.

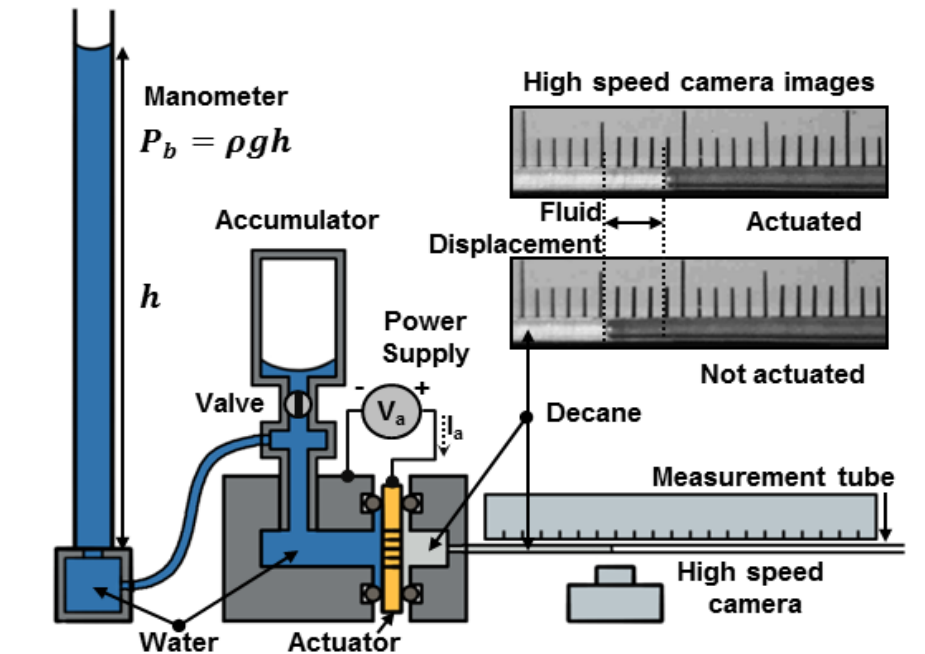


Figure 6. Experimental Setup

The setup consists of the following components filled with their respective liquids, in Table 4.

Table 4. Parts of Actuator Test Setup

$i$	Part	Fluid
1	Manometer	NaCl
2	Tubing	NaCl
3	Accumulator	NaCl
4	Assembly (water side)	NaCl
5	Actuator	NaCl/Decane
6	Assembly (oil side)	Decane
7	Measurement tube	Decane

With length and diameter known for each  $i$ th component, the total system resistance was calculated as

$$R_s = \sum R_i$$

For the pressure sources, the manometer and tubing are parallel to the accumulator, and the equivalent resistance for these sections was calculated accordingly. Using the dynamic model developed earlier,  $f_{max*}$  can be approximated.

In testing, the key operating parameters were the back pressure, actuation frequency, and voltage. Experimentation over various parameter combinations revealed that higher back pressures and voltages produced greater  $V_{disp}$  and power.  $P_b$  should be at least half  $P_{max}$ . At frequencies beyond the predicted  $f_{max*}$ , the observed displacement gradually decreased, as expected. Though a higher voltage initially produced larger displacements, it caused a relatively

quick degradation in displacement over time. Detailed experimental and analysis procedures can be found in [1].

### 3.5 Reliability

It was noticed that the actuation volume would degrade slightly over time, calling into question the reliability of MEAs. Tests were performed on 25  $\mu\text{m}$  D plates at various voltages to observe repeated electrowetting performance over tens of thousands of actuation cycles. Two actuation cycles result from each electrical cycle, with displacement happening at the waveform peak and trough. Figure 7 shows the reliability test results for sine wave excitation below  $f_{max*} \approx 40 \text{ Hz}$  and  $P_b = 3.5 \text{ kPa}$ .

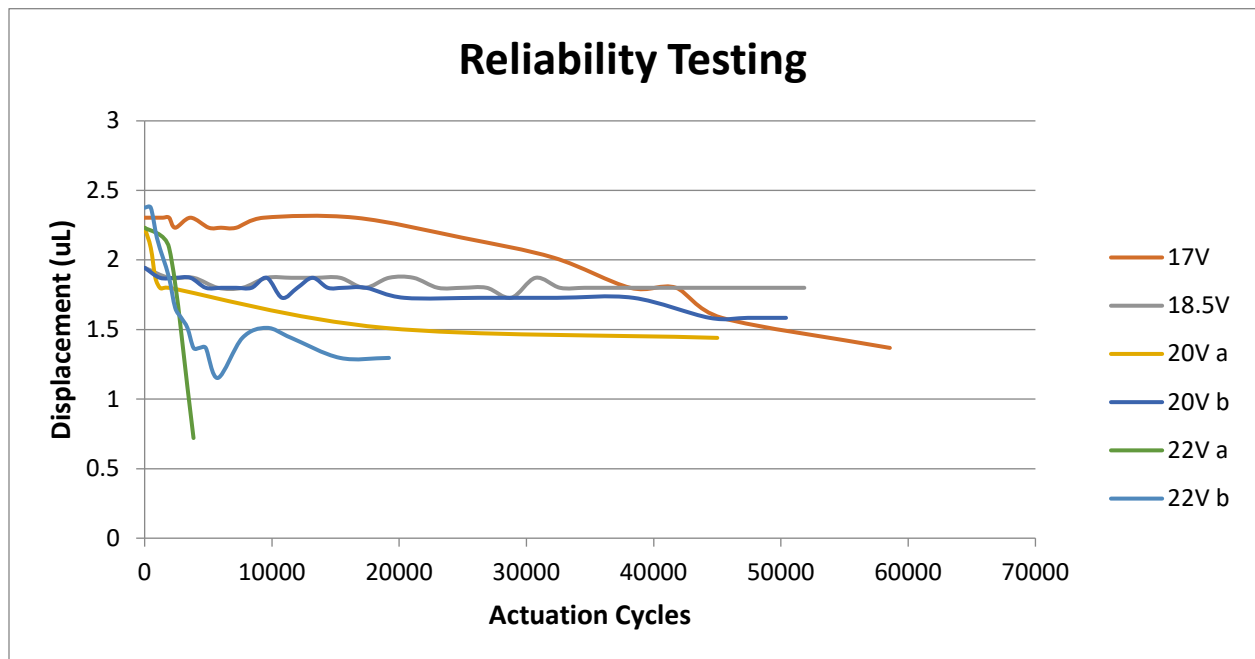


Figure 7. Reliability Testing

As suspected, higher actuation voltages produce on average a larger volumetric displacement at the cost of a quicker drop-off in performance. The lower voltages still produced

a considerable initial displacement around 2  $\mu\text{L}$ , only slightly below that of the higher voltages. Over many cycles, the actuation curves corresponding to 20 V and below flattened out toward a displacement of about 1.7  $\mu\text{L}$ , with little signs of further degradation beyond this range.

The suspected reason behind degradation in reversible electrowetting is charge trapping within the Cytop dielectric, which effectively decreases the average applied voltage across the actuator. A similar degradation is observed by [16], who tested repeated electrowetting on three different dielectric fluoropolymers, with Cytop having the best performance. They propose that the electrically leakier Cytop allows trapped charges to diffuse more easily. Another contributor to degradation is local dielectric breakdown at higher electric fields, such as for the case with a 22V applied voltage where steep degradation rates are observed.

As long as higher actuation voltages above 20 V are not applied over long durations, MEAs remain a consistent and reliable option worth exploring for microrobotics.



# Chapter 4      Squid Design

After experimentally verifying the microhydraulic electrowetting actuator's potential for reliable actuation, the next step was its implementation into a mini-robotic system. The design goal was to create a robotic platform to demonstrate MEA-driven propulsion at velocities comparable to marine organisms at the centimeter length scale. Throughout the design process, emphasis was placed on fabrication simplicity which led to the adoption of additive manufacturing processes. It will be seen that individual component design variables have an interconnected influence on performance, despite the linear fashion in which the component design process is presented. Multiple variants were proposed but only the final design is presented here. The following discussion of the squid design consists of concept generation, analytical modeling, and system development.

## 4.1 Inspiration

Since microhydraulic actuators are particularly well-suited for fluid-immersed environments, inspiration for a mini-robotic platform was naturally drawn from the sea. Animals belonging to the Cephalopoda class, including squid and chambered nautilus, are known to utilize a combination of undulatory fin motion and jet propulsion for biolocomotion, depending on the specific task. Studies of biolocomotive efficiency of long-finned and brief squid through ontogeny show that paralarvae rely almost exclusively on a high-frequency, low velocity jet for movement until growing to a 1.5 cm mantle length, reaching speeds of up to 16 cm/s [17]. A

peak propulsive efficiency of 40% is achieved at 1 cm mantle length [18]. Such studies confirm jet propulsion is a viable locomotion mechanism at centimeter length scales and below.

## 4.2 Propulsion Scheme

Jet propulsion in squid can be described in part by momentum transfer via diaphragm pumping. In a diaphragm pump, a reciprocating diaphragm first deflects to increase the pump chamber volume, which decreases the internal pressure causing fluid to flow inwards through an inlet (suction phase). Next, the diaphragm deflects in the opposite direction, reducing the chamber volume and ejecting fluid through an outlet (pump phase). Check valves maintain directionality of the flow by preventing backflow. Without check valves, a squid expands its mantle to suck water into its body through an aperture. When the mantle contracts, a water jet is expelled through the same aperture, now constricted, at a higher velocity than it entered with. The momentum difference between the incoming and outgoing jets imparts a net propulsive force onto the squid. It is recognized that other effects play a role in squid jetting, such as vortex ring interactions and induced coflow, but these are assumed to play a less significant role when analyzing pulsatile jets through two designated (inlet and outlet) orifices.

In similar fashion to the diaphragm pump, the MEA can be used to hold a “liquid diaphragm” that sucks in and expels fluid through a chamber. The positioning of passive check valves at the inlet and outlet will ensure unidirectional flow while eliminating the need for active control, thus reducing complexity. The orifice diameters and valve orientation can be designed for the jet to impart optimal thrust.

## 4.3 Actuator Configuration

When analyzing possible actuator configurations for the squid, valuable insight was gained from research in synthetic jet actuators (SJA). SJA are used primarily in aeronautical systems for flow control, heat transfer, and jet vectoring. They form jets “entirely from the working fluid of the flow system in which they are deployed and, thus, can transfer linear momentum to the flow system” [19]. Double-acting operation is commonplace for SJAs, and is described as an actuator that “consists of two... chambers, from which fluid is displaced by the opposite sides of the same diaphragm” [20], such that the chambers are pumped intermittently in anti-phase with each other.

In designing the mini-robotic squid, two actuator configurations were considered:

Configuration A is a single acting arrangement identical to a diaphragm pump, consisting of a single actuator covered by a deformable membrane that flexes to accommodate volume displacement. Throughout expansion and contraction, the membrane supplies a relatively constant back pressure to the actuator. On the other side of the actuator plate is the pumping chamber, or mantle, with check valves positioned at the inlet and outlet to dictate the flow direction. The membrane can supply positive pressure or negative pressure, depending on the arrangement of oil and water (NaCl). An example of this configuration is shown below.

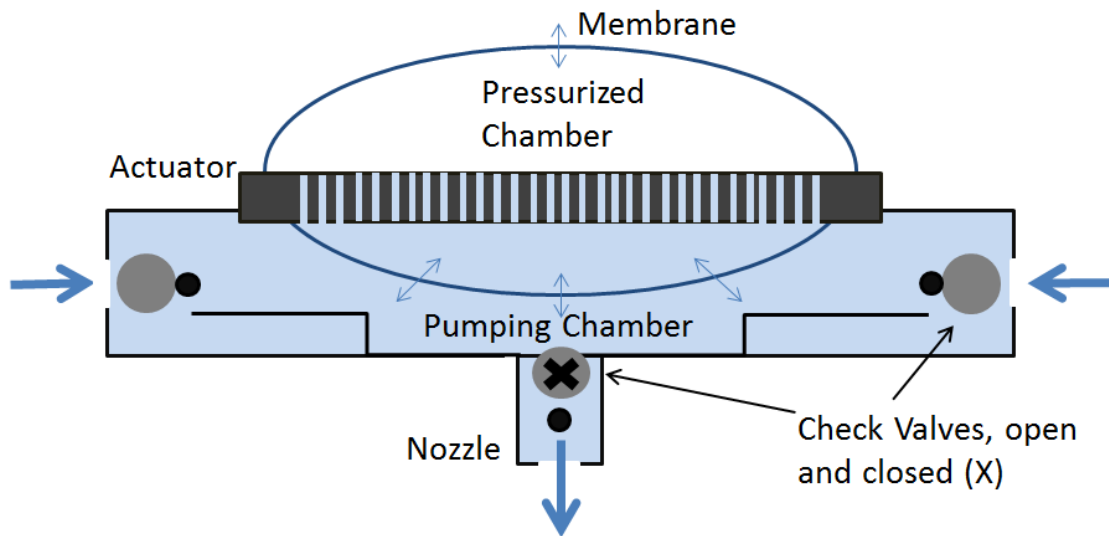


Figure 8. Single-Acting Arrangement

Configuration B is a double-acting arrangement that uses two actuators, symmetric about a shared pressurized water chamber. There are two separate but parallel pumping chambers, each adjacent to an actuator. The actuators operate in anti-phase: as the first ( $V_{OFF}$ ) expels water, the second ( $V_{ON}$ ) takes in water with an enhanced back pressure of  $P_{max}$  supplied by its inactive counterpart, and so forth. No deformable membrane is needed since back pressure is derived from the actuators' capillary pressure.

The comparative advantages of the double-acting configuration are examined:

#### Advantages

- allows for simple, symmetric design
- eliminates need for deformable membrane
- higher potential volume efficiency  $\eta_{volume}$
- higher theoretical back pressure and driving pressure

#### Disadvantages

-larger device size, more skin friction drag

-possibility of complex dynamic coupling effects between the actuators

Volume efficiency  $\eta_{volume}$  is defined as the ratio of actuator active volume to total device volume with  $n$  actuators.

$$\eta_{volume} = \frac{V_{active}}{V_{total}} \approx \frac{nV_{disp}}{V_{total}}$$

The supporting structure consists of valves, the pumping chamber, and a shared water chamber with a volume of at least  $V_{displacement}$ . The maximum volume efficiencies for both configurations are calculated as

$$\eta_{volume_A} = \frac{V_{active}}{V_{actuator} + V_{support} + V_{displacement}}$$

$$\eta_{volume_B} = \frac{2V_{active}}{2(V_{actuator} + V_{support}) + V_{displacement}}$$

Having a shared water chamber reduces the total volume in configuration B by  $V_{displacement}$ . Otherwise, as in configuration A, there would need to be a membrane with minimum capacity  $V_{displacement}$  to accommodate volumetric displacement, per actuator.

Another benefit of double-action is having back pressure supplied by capillary pressure  $P_{max}$  from hydrophobic capillaries, which equates to an increase in driving pressure by a factor of 2 in theory. Under configuration A, the pressure fraction is close to  $\frac{1}{2}P_{max}$ , to allow equal magnitude of driving pressure in meniscus extension and retraction through the actuator plate. In double-action, as long as an oil-water interface remains in the inactive actuator's capillaries, a back pressure of  $P_{max}$  is delivered to the active actuator.

$$P_{back_A} = F_P P_{max} = \frac{1}{2} P_{max}$$

$$P_{back_B} \approx P_{max}$$

Configuration B was selected for its advantages in volume efficiency and pressure. Without the need for a flexible membrane, fabrication is made simpler while the additional complexities seem manageable and do not drastically change the fundamental operation of the squid.

## 4.4 Stacking Architecture

The design process was focused on optimizing the propulsive force, thus maximizing velocity. Given the flat form factor of the MEA plates, it was logical to adopt a stacking approach to building the squid, where components are laid horizontally on top of each other, as in Figure 9.

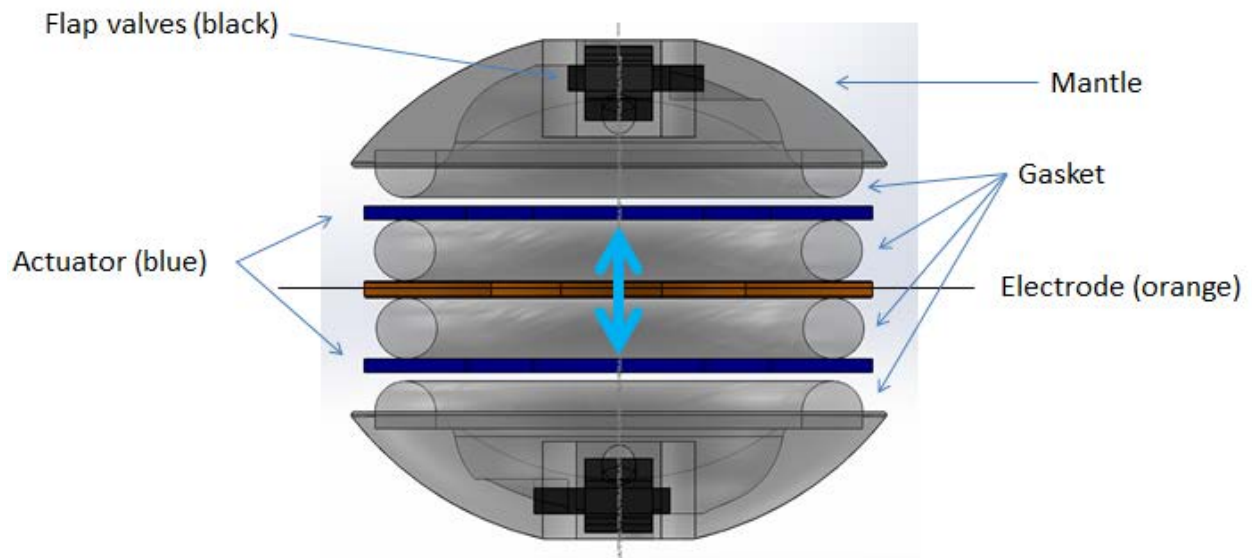


Figure 9. Double-Acting Squid Robot (back)

The robotic squid is comprised of a stack of individual components. Two parallel pump chambers, or mantles, lie symmetrically about a shared water chamber, which is located between dual actuators operating in anti-phase. The stack is compressed together by heat-shrink tubing and

hydraulically sealed at the gaskets. A buoy is attached to the squid for flotation when it is immersed in decane. Both the compression tubing and buoy are not pictured in Figure 9.

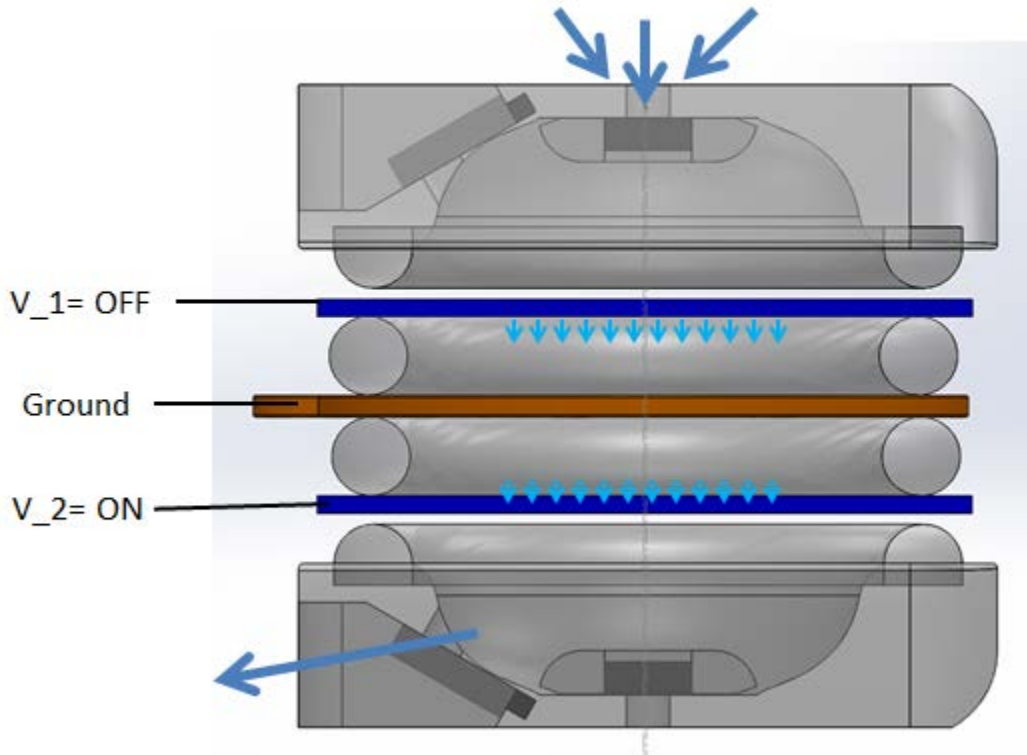


Figure 10. Double-Acting Squid Robot (side)

In Figure 10, the fluid flow path can be seen running through the components in the following order: inlet orifice, inlet valve, top mantle cavity, top actuator, water chamber, bottom actuator, bottom mantle cavity, outlet valve, and outlet orifice.

In subsequent sections, the design considerations and development of each subcomponent are discussed in detail, beginning with the actuator.

## 4.5 Actuator

The 25  $\mu\text{m}$  D actuators were selected to drive the squid. The selection of an actuator fixes the power density, driving pressure, displacement volume, and general size of the squid. While higher pressures are produced at 10  $\mu\text{m}$  D, there is only half as much displacement volume, which may complicate the check valve design. The 25  $\mu\text{m}$  D actuator dimensions are given in Table 5 and shown in Figure 11.

Table 5. Actuator Specifications

Capillary D	25 $\mu\text{m}$
Capillary stop D	10 $\mu\text{m}$
Capillary Length L	200 $\mu\text{m}$
Aspect Ratio L/D	8:1
Actuation volume $V_{\text{disp}}$	5-7 $\mu\text{L}$
Number of capillaries	60k
$P_{\text{max}}$ theoretical	8 kPa
$P_{\text{bleed}}$ theoretical	16 kPa



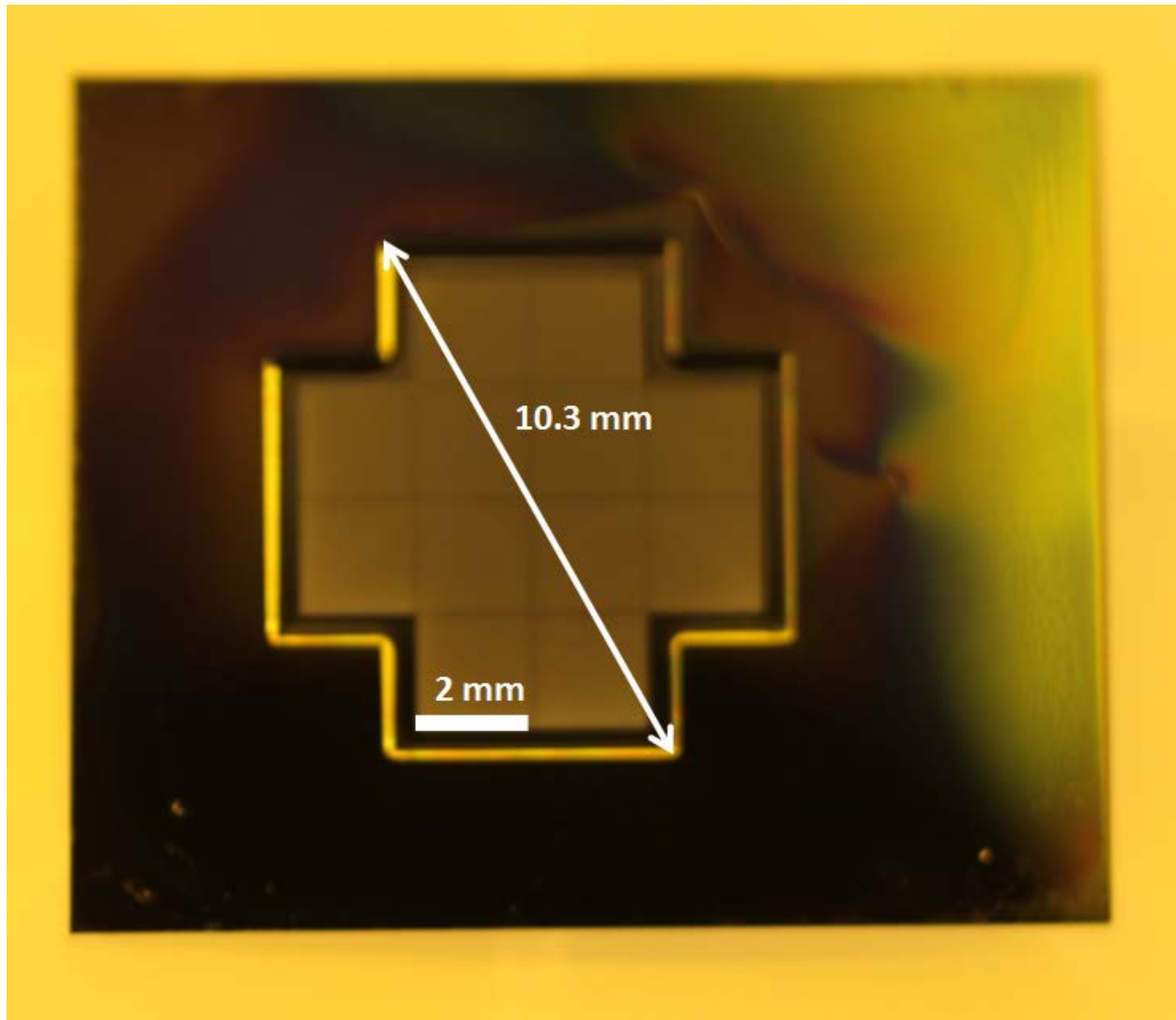


Figure 11. Actuator, 25  $\mu\text{m}$  D (backside)

The cross-shaped porous region in the middle is composed of 12 smaller porous squares measuring  $2 \times 2 \text{ mm}^2$  that lie within the area of an  $8 \times 8 \text{ mm}^2$  square. The front of the actuator plate is flat, while the back contains an indented region resulting from the backside etch, thinned down from  $450 \text{ }\mu\text{m}$  to  $200 \text{ }\mu\text{m}$ . The indented region on the backside extends outward  $0.5 \text{ mm}$  from the capillary squares, falling within the area of a  $9 \times 9 \text{ mm}^2$  square. The longest diagonal across the indented region is  $10.3 \text{ mm}$ . This poses a requirement that the gasket sealing the backside must have a diameter greater than  $10.3 \text{ mm}$  to fully engage the active capillary region.

The actuator dies are diced from  $20 \times 20 \text{ mm}^2$  down to  $18 \times 15 \text{ mm}^2$ . This was done to leave enough assembly tolerance for gasket placement around the active region and to offer more area on the sides when securing electrical interconnections to the actuator plates, which is discussed later.

## 4.6 Electrical Waveform

Although the double-acting actuators operate in anti-phase, the voltage signals applied to them must be in quadrature, shifted by  $90^\circ$ . This is depicted in Figure 12 where two 20 V sine waves are shown with five time markers. The orange wave precedes the blue waveform by a quarter-cycle, or  $90^\circ$ . At point 1, the “blue actuator” receives  $V_{blue} = 20V$  from the blue waveform, and is fully actuated in the ON state. At the same time,  $V_{orange} = 0V$  and the “orange actuator” is in the OFF state. At point 2, a quarter cycle has passed, and now the blue actuator is OFF ( $V_{blue} = 0V$ ) while the orange actuator is ON ( $V_{orange} = -20V$ ). During the transition from point 1 to 2, the blue actuator forced water out of its capillaries at pressure  $P_{max}$  into the orange actuator which then had  $\Delta P = 0$ . Continuation of this double-action cycle results in this same actuation pattern.

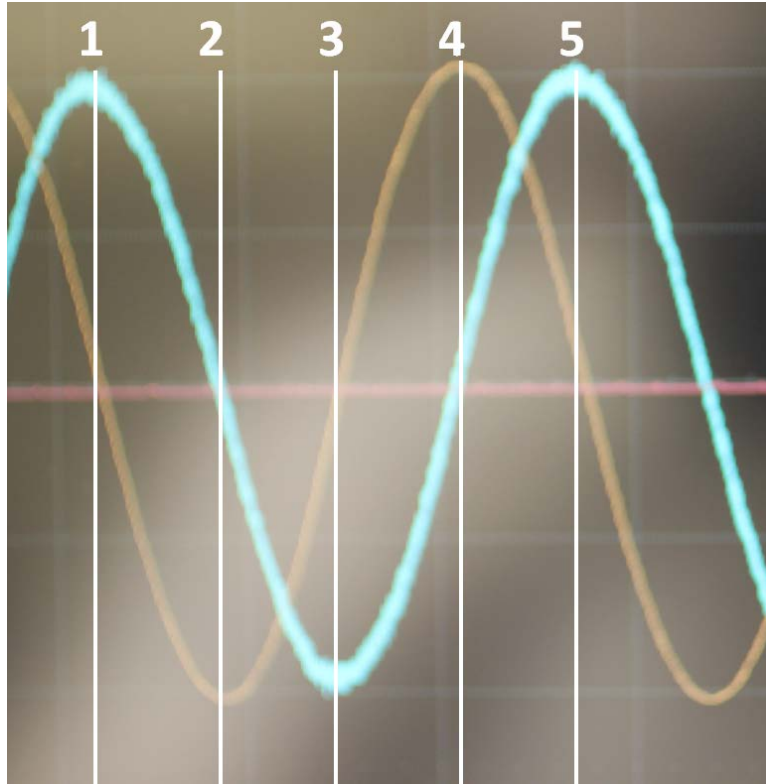


Figure 12. Quadrature Waveforms

A quadrature circuit was constructed using a sine wave from an arbitrary function generator (Hewlett Packard 8116A Pulse/Function Generator 50 MHz) as the input signal. Data was acquired by an oscilloscope (Teledyne LeCroy WaveRunner 104 MXi 1 GHz Oscilloscope). A second voltage waveform in quadrature was generated by feeding the input through a first-order all-pass filter. An all-pass filter introduces a phase shift at unity gain. Only a single op-amp is needed; an OPA445 high-voltage operational amplifier was used in the all-pass filter. For a specific frequency  $\omega = 2\pi f = 1/RC$ , the input waveform undergoes a  $90^\circ$  phase shift. The circuit resistive load is a potentiometer that allows tuning of the quadrature frequency.

## 4.7 Modeling

The performance prediction of the robotic squid is meant to provide an expected range for the squid velocity  $U_{squid}$ , and is based on the same method used for modeling the actuator. In the double-acting configuration, the serial fluid path passes through the squid as shown in Figure 10.

With the two actuators operating in anti-phase, the driving pressure to one actuator is supplied by the positive expelling capillary pressure from the other actuator. Since fluid displacement  $V_{disp}$  is the same in both actuators,  $P_s$  will become zero when the receding meniscus in the inactive actuator reaches the capillary openings. Because both actuators share the same displacement, the advancing meniscus into the active actuator cannot be driven past the capillary stop, thus water bleed-through is improbable. Bleed-through is, however, possible in the case that a significant number of capillaries in one actuator become clogged, such that for the other actuator the fluid intake per capillary increases beyond the capillary volume.

The back pressure is supplied by the actuator in which water is receding.

$$P_b \approx P_{max}$$

The system hydrodynamic resistance is calculated as

$$R_s = \sum R_i = 2R_{act} + 2R_{orifice} + R_{mantle} + R_{chamber} + 2R_{valve}$$

For circular orifices of diameter  $d$  with mantle wall thickness  $t$ :

$$R_{orifice} = \frac{128\mu t}{\pi d^4}$$

An estimate of component resistances from preliminary testing shows that the check valve resistance  $R_{valve}$  dominates  $R_s$ .

Propulsive thrust is derived from a control volume approach assuming no leakage, constant jet velocity, and steady flow conditions for continuous operation. Modeling the squid as having outlet orifices oriented coaxially along the thrust direction, and inlet orifices orthogonal to the outlet orifices, the propulsive force can be simplified to

$$F_{thrust} = \dot{m}(U_2 - U_1) = \dot{m}U_{jet}$$

$$\dot{m} = \rho AU = \rho 2V_{disp}f_{max}$$

$$Q = A_{orifice}U_{jet}$$

where  $\dot{m}$  is mass flow rate and  $Q$  is volumetric flow rate with  $U_{jet}$  as jet velocity. The factor of 2 in  $\dot{m}$  accounts for double-action. The inflow enters through opposite facing inlet orifices and produces zero net momentum flux. The velocity  $U$  can be rewritten as

$$U_{orifice} = \left( \frac{Q}{A_{orifice}} \right) = \frac{2V_{disp}f_{max}}{A_{orifice}} = \frac{P_s}{R_s A_{orifice}}$$

Substituting for thrust gives

$$t_{fill} = V_{disp}/Q_{ss}$$

$$F_{thrust} = \rho 2V_{disp} \left( \frac{1}{2t_{fill}} \right) \left( \frac{P_s}{R_s A_{orifice}} \right) = \rho 2V_{disp}f_{max} \left( \frac{P_s}{R_s A_{orifice}} \right)$$

$$A_{orifice} = \pi d_{orifice}^2/4$$

For maximum thrust, the orifice should be designed to maximize outgoing jet velocity. With a fixed mantle wall thickness, the orifice diameter should be decreased to increase jet velocity, up to the point where further shrinking of the orifice significantly increases  $R_s$  such that the jet velocity begins to decrease. With ideal valve checking performance, the orifice diameter should be set to satisfy the relation:

$$\frac{\partial F_{thrust}}{\partial d_{orifice}} = \left( \frac{\partial F_{thrust}}{\partial R_s} \right) \left( \frac{\partial R_s}{\partial d_{orifice}} \right) + \left( \frac{\partial F_{thrust}}{\partial A_{orifice}} \right) \left( \frac{\partial A_{orifice}}{\partial d_{orifice}} \right) = 0$$

The peak velocity of the squid is reached when the drag force is equal to thrust.

$$F_{drag} = \frac{1}{2} \rho_{oil} U_{squid}^2 C_d A_{squid}$$

Here  $C_d$  is drag coefficient and  $A_{squid}$  is the wetted frontal area. A drag coefficient of 1.15 was used for a short cylinder oriented perpendicular to the flow.

## 4.8 Mantle

The mantle is a covering that protects and provides structural support for internal components. The robotic squid's mantle pieces are located at the top and bottom of the stack architecture, though they do not completely envelop the inner components. The remaining components are sandwiched in between the mantle halves under compression tubing.

Several CAD iterations were created using SolidWorks, with the following design considerations:

**-Size:** Size should be optimized for drag and weight reduction, as the mantle is one of the heaviest parts of the squid assembly. It must envelop the entire active capillary region of the actuators, but shouldn't be much larger beyond that. There must also be room for the check valves and orifices to fit onto the mantle.

**-Shape:** A more streamlined profile will help to reduce the drag force and increase squid velocity. Additionally, the inlet and outlet check valves are located inside and outside the mantle, respectively. A flat area should be designated for valve placement. Valves and orifices must be correctly oriented for efficient momentum transfer to the oil surrounding the squid. In order to concentrate the exit jet momentum, the outlet valve should be placed into a recessed valve fixture where the sidewalls confine the jet direction.

**-Hydrodynamic resistance:** This should always be minimized for maximal thrust. The channel in the mantle cavity should not be a major contributor to the flow path resistance, as it is one of the larger components. However, the orifice and check valve, which are both integrated with the mantle, are expected to be highly resistive.

**-Wall thickness:** The thickness of the walls must withstand pressures that are both internally generated and that result from outer compression. As long as the mantle is robust during the assembly procedure, thickness can be reduced. The mantle deflection under driving pressure  $P_s$  should not reduce the ejected volume.

**-Interfacing:** The gasket and compression tubing will be pressed against both sides of the mantle. Special features may be incorporated to help with the assembly process. Enough room should be left between the two mantle pieces for electrical connections to the actuators.

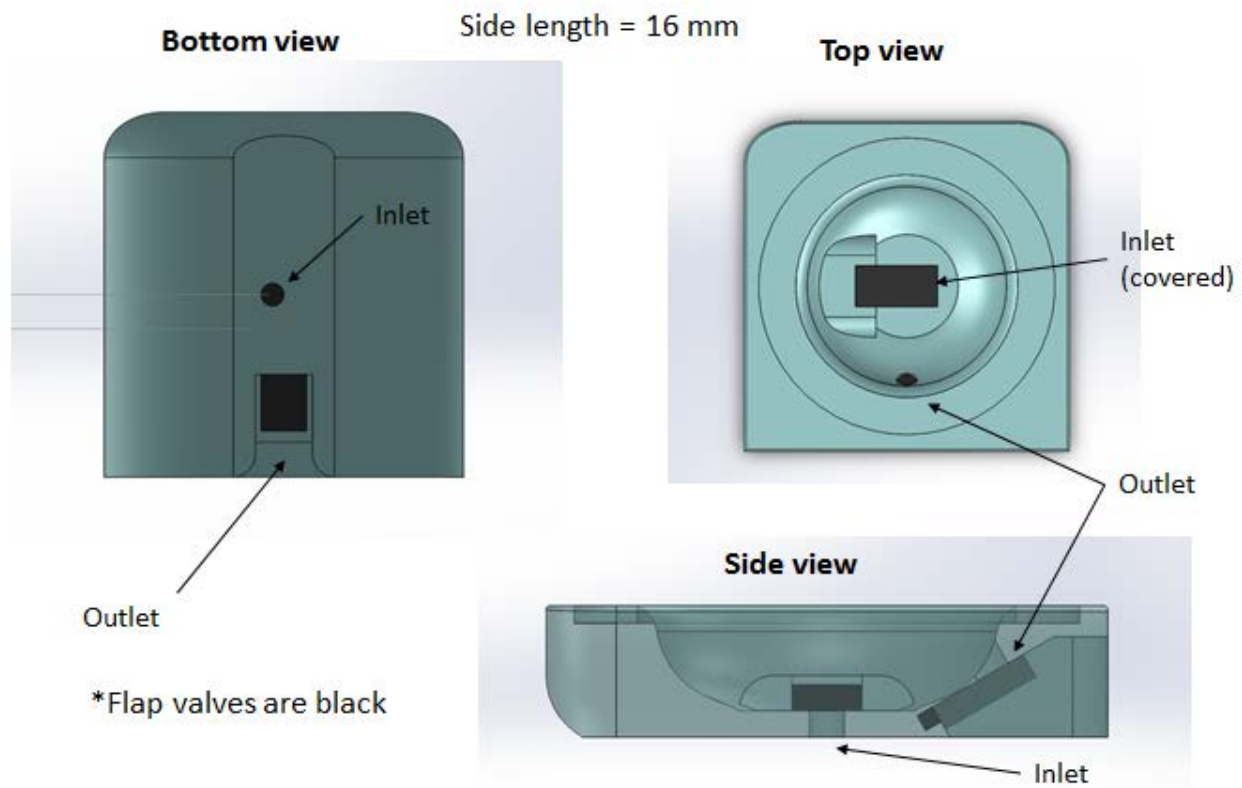


Figure 13. Mantle Design (multiple views)

Figure 13 shows the finalized mantle design in green, with the check valves represented in black. The valve fixtures and orientations are positioned so that the incoming jets are perpendicular to the outgoing jets. From the top view, an annular groove is designed as a gasket seat. Seen in Figure 9, the outside portion of the mantle is rounded for sliding into the compression tubing, but flat at the bottom for stability on flat surfaces, which is important during assembly. Lastly, the material outside of the annular groove could be further reduced, but it also serves to provide support underneath the gaskets during compression to ensure the underlying material does not deflect. Otherwise, the gaskets may not properly form a hydraulic seal.



## 4.9 Gasket

The purpose of the gasket is to form a hydraulic seal at the component interfaces. They are placed around both actuators. Desired characteristics of the gasket are:

- chemical resistance to NaCl, oils, and cleaning solvents
- compliant, low modulus of elasticity
- envelop actuator capillary region ( $ID > 10.3 \text{ mm}$ )
- facilitates water injection into the chamber between actuator plates

The gasket design was modeled after an AS568 013 O-ring, with inner diameter  $ID = 10.82 \text{ mm}$  and circular cross-sectional diameter  $(OD - ID) = 1.78 \text{ mm}$ . TangoPlus, a rubber-like material compatible with 3D-printing was chosen as the gasket material. It has an estimated elastic modulus of  $E = 0.6 \text{ MPa}$ , which is lower than those of Viton and Buna rubbers commonly used to mold O-rings.

To inject NaCl in between the actuators, a small needle is inserted through the gasket to access the shared water chamber. Before assembly, a gauge 32 biopsy tool is inserted through the gasket. The core is removed before proceeding with assembly. Water injection occurs after the stacked assembly has been compressed and immersed in decane, and after air has been purged from within. The now-compressed gasket forms a hydraulic seal around the biopsy tool.

Pressurized injection of NaCl ensures the water chamber and actuator capillaries are filled with enough water to allow full volumetric actuation of a single MEA. The injected volume is set equal to the actuator displacement volume plus the water chamber volume. The back pressure during injection is decided based on the actuator capillary curve, which indicates a pressure of 8 kPa will fill each actuator with  $3 \text{ }\mu\text{L}$ , or half of  $V_{disp} \approx 6 \text{ }\mu\text{L}$ . After injection, the biopsy tool is removed from the chamber, creating a temporary vacuum in the formerly occupied space. The

hole in the gasket is quickly closed off by compressive forces. Calculations were performed to ensure the water volume is not severely impacted by biopsy tool removal.

The gauge 32 biopsy tool has OD = 0.24 mm and ID = 0.11 mm, and an inserted length of  $L_{needle} = 2 \text{ mm}$ . The volume change is  $V_{needle} = \pi \left( \frac{OD^2 - ID^2}{4} \right) L = 0.07 \text{ } \mu\text{L}$ , which is small compared to the actuation displacement.

$$\frac{V_{needle}}{V_{disp}} \approx \frac{0.07}{5} < 2\%$$

## 4.10 Electrode Plate

The purpose of the electrode plate is to ground the input waveforms transmitted from the two actuator plates. It is linked to the MEAs via 0.01 M NaCl solution acting as a liquid electrode. In the assembly, it is directly bordered by two gaskets. The conductive plate should be designed to be lightweight, rigid under compression, and resistant to corrosion. If it is too thin like aluminum foil, a slight misalignment of the surrounding gaskets can cause the assembly to buckle in compression.

Aluminum was selected as the electrode material for its high strength-to-weight ratio. A custom-shaped ring was formed from 6061-T6 aluminum sheet metal, shown with a gasket in Figure 14.

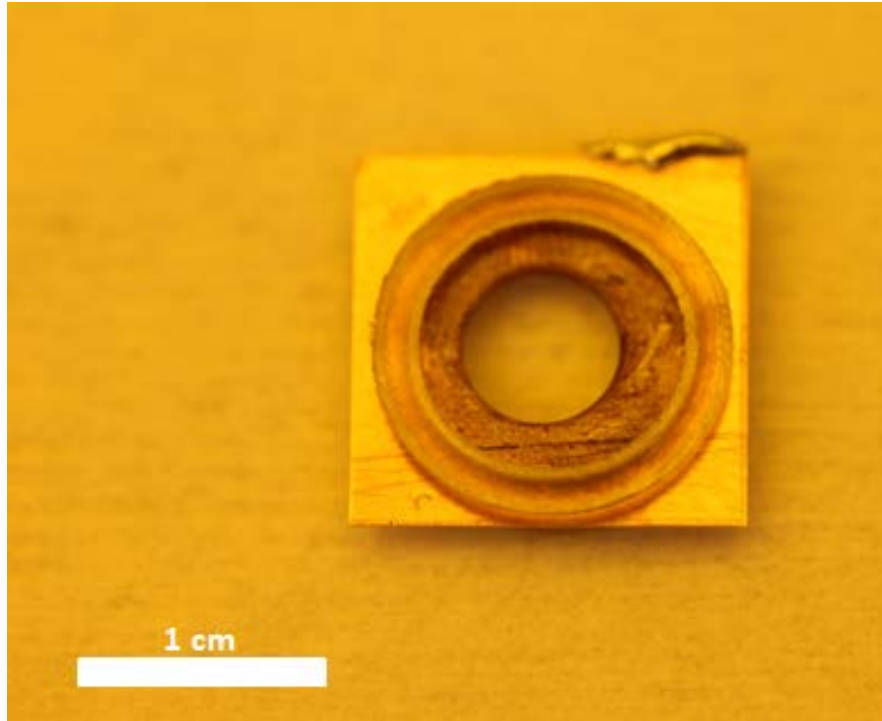


Figure 14. Electrode plate with O-ring

However, a conductive metal ring may not be suitable for continuous, long-term operation. Since electric current passes through the ring, oxidation occurs at the surface, generating oxygen and rust that can clog the actuator capillaries and degrade electrowetting behavior over time. However, a dielectric-coated capacitor plate designed to exploit capacitive coupling would be a viable long-term solution. An electrical circuit model of the robotic squid's electrically-active components was created in MATLAB to simulate the voltage waveforms applied across the MEAs, using a dielectric-coated capacitor plate in place of the metal plate, shown in Figure 15.

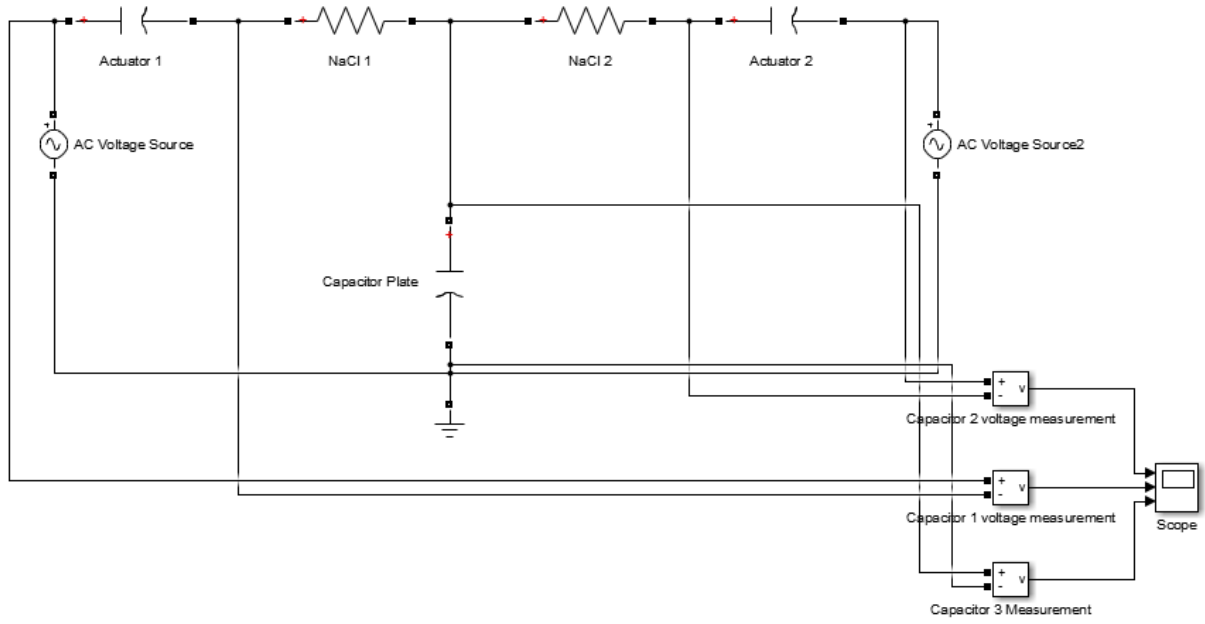


Figure 15. Squid Electrical Circuit

The impedance of NaCl as a fluid electrode is generally several orders of magnitude smaller than the reactive capacitive impedances  $X_C$  at actuation frequencies up to  $f_{max}$ , near 50 Hz. The electrical impedance of the fluid electrode is

$$R_{fluid} = \frac{\rho L}{A} \ll X_C$$

with  $\rho$  the resistivity,  $L$  length, and  $A$  cross-sectional area. The resistivity of NaCl varies with concentration since  $\text{Na}^+$  and  $\text{Cl}^-$  are strong electrolytes, but is relatively low ( $\sim 10 \text{ k}\Omega$ ). The remaining resistive elements include lead wires ( $\sim 1 \text{ }\Omega$ ) and actuators ( $\sim 1 \text{ k}\Omega$ ). Thus the unreactive resistive elements are negligible compared to the capacitive impedances ( $\sim 1 \text{ M}\Omega$ ) and can thus be neglected.

The circuit model can be considered a simple capacitive voltage divider in which the voltage drop across the capacitive electrode plate can be estimated using superposition. Ideally, to preserve low-voltage operation and actuation efficiency, the majority of the voltage drop

should occur across the actuators while keeping the voltage across the capacitor electrode plate at a minimum.

Capacitors are reactive components, and as such their impedances  $X_c$  are dependent on frequency as

$$X_c = \frac{1}{j\omega C} = \frac{1}{j\omega} \left( \frac{d}{\epsilon_0 k A} \right)$$

with dielectric thickness  $d$ , permittivity of free space  $\epsilon_0$ , dielectric constant  $k$ , and surface area  $A$ .

The impedance of each MEA is on the order of  $M\Omega$ . For each AC voltage source, it is seen that voltage will be divided among an actuator and the electrode plate, based on their relative impedance magnitudes. According to voltage division, the voltage drop  $V_0$  across an element with impedance  $Z_0$  is

$$V_0 = V_{source} \left( \frac{Z_0}{Z_{total}} \right)$$

$$Z_{total} = Z_0 + Z_A // Z_B$$

where “A//B” denotes the impedance of parallel elements A and B.

Taking the voltages applied to the actuators  $V_1, V_2$  and electrode plate  $V_3$ , in a circuit with one voltage source and actuator, the drop across the electrode plate is:

$$V_3 = V_{source} \left( \frac{Z_3}{Z_{total}} \right)$$

Then for a circuit having two voltage sources in quadrature, the superposed voltage drop  $V_{3*}$  can be approximated as

$$V_{3*} \approx \sqrt{2V_3^2}$$

All significant components are reactive, and therefore voltage division is independent of frequency.

In order to attain the maximal voltage drop across the actuators, the electrode capacitance  $C_3$  must be minimized relative to the actuator capacitances  $C_{1,2}$ . Practically,  $C_3$  should be at least an order of magnitude greater than  $C_{1,2}$ , which has a theoretical maximum of 159 nF.

When designing for the electrode plate, the strategy was to minimize weight by controlling ring height and inner diameter. The inner diameter has to be smaller than the gasket ID for proper sealing, while the voltage across the electrode dielectric could not exceed the dielectric breakdown field. For increasing capacitance, options considered in addition to materials selection included adding pores to create more surface area.

Hafnia was chosen as the dielectric for its high dielectric constant and high breakdown field. The breakdown field of hafnium oxide increases as the film thickness decreases; a film 125 Å thick has an average breakdown field of about 500 V/μm.

The requirements for a working design were an actuator voltage drop  $V_{1,2} > 20\text{ V}$  using  $V_{source} < 30\text{ V}$  without dielectric breakdown. A working design for future use was found using a 10 nm hafnia-coated ring with height  $h = 1\text{ mm}$  and ID = 3.5 mm, although there are many possible solutions. The relevant parameters of this design are shown in Table 6.

Table 6. Electrode plate design parameters

$V_{source}$ (V)	$V_1$ (V)	$C_3/C_{1,2}$	$V/d$ (V/μm)
30	28.9	45.8	158
25	24.1	45.8	131.4
20	19.3	45.8	105.1

## 4.11 Sealing

After all components are stacked, the assembly must be sealed to prevent fluid leakage. Heat shrink tubing was the method chosen for compression sealing. By fitting a section of heat shrink tubing over the assembly, clamping, and then applying heat, a hydraulic seal can be formed to withstand upwards of 10 kPa inside pressure. In general, the gasket compression pressure should exceed the pressure difference across the gasket. Dual-walled semi-rigid XLPO (cross-linked polyolefin) tubing with an expanded ID of  $\frac{3}{4}$ " was selected for its rigidity, above-average shrink ratio (2.5:1), and relatively low shrink temperature of 140°C.

When heated past its minimum shrink temperature, the polyolefin tubing conforms to the shape of the assembly. The unheated assembly including heat shrink tubing must be clamped to deform the O-ring gaskets. After compression, the deformed gaskets rebound only slightly. The amount of rebounding is governed by equilibration of the gasket compression pressure/force and the shrink tubing's hoop stress. If the gasket is too stiff to sufficiently deform, the gasket compression pressure will be highly sensitive to stretching of heat shrink tubing. For example, if there is only 0.1 mm of compression, a 0.1 mm rebound in assembly length will completely eliminate sealing.

## 4.12 Buoy

The components described thus far are constructed of materials denser than decane. Thus a buoy is needed to keep the robotic squid assembly afloat. The buoyancy force is equal to the weight of the volume of displaced fluid. An expanded polystyrene (Styrofoam) buoy of volume  $V_{buoy}$  can be attached to the side of the assembly. Styrofoam has a density of 100 kg/m<sup>3</sup>, which

is about seven times less than that of decane. All significant reductions in size were made in previous components to decrease the size requirement of the buoy. The minimal required size of the buoy was calculated based on a summation of forces along the vertical axis:

$$F_{squid} = \sum_i (\rho_{oil} - \rho_i) V_i g < 0$$

$$F_{bouy} = (\rho_{oil} - \rho_{bouy}) V_{bouy} g > 0$$

$$F_{bouy} + F_{squid} > 0$$

$$V_{bouy} > -\frac{F_{squid}}{(\rho_{oil} - \rho_{bouy})g}$$

Summing the component weights resulted in a required buoy volume of 1.9 cm<sup>3</sup>.

## 4.13 Interconnects

The following requirements were made for the electrical interconnects to the actuators and electrode plate:

**-High Compliance:** The force exerted on the floating squid by the interconnecting wires can restrict its movement. To avoid constrained movement, thin gold bonding ribbon was chosen to make the connections.

**-Secure Connection:** The electrical connections should be made as the last step in the assembly process so that the bonding ribbon does not become a hindrance during assembly. Since it is difficult to reliably solder onto silicon, compression-based methods are the choice method to maintain robust electrical contact.



A reliable method to create secure connections is to insert a slice of O-ring material in between the actuator and electrode plate after assembly compression, with bonding ribbon on either side of the piece. The side that the ribbon is placed on depends on the component the ribbon is intended to form an electrical connection with. The narrow gap between the actuator and electrode plate squeezes the slice, which holds the bonding ribbons tightly against their respective metal contact surfaces.

## 4.14 Check Valve

The check valve performance is strongly influenced by the orifice diameter and pressure applied across the valve. This section reports the check valve selection process and design.

### Valve Selection

The check valve controls the directionality of flow entering and exiting the robotic squid. Its function is to permit flow in only one direction and is measured by diodicity  $Di$ , the ratio of forward flow to reverse flow.

$$Di = \frac{Q_{forward}}{Q_{backward}}$$

Many types of MEMS check valves have been developed for various applications. [21] presents a review of micro check valves and lists their reported forward and reverse flowrates. An ideal check valve for the squid would have a high  $Di$ , fit reliably onto the mantle, have low resistance to flow, and be 3D-printable. The many varieties of passive check valves were down-selected to the flap valve according to the aforementioned design criteria. Other common types included membrane, ball, diffuser, and capillary valves, but they are either too resistive or not as efficient (low  $Di$ ). There are quite a few sub-types within the flap valve category. In the end, the

cantilever-type valve was chosen as the most viable for its simplicity, design flexibility, and small size. It is composed of a flexible cantilever covering an orifice while attached to a rigid base. The operation of a cantilever-type flap valve is shown in Figure 16. Under positive pressure, the cantilever deflects away from the orifice, opening a path for forward fluid flow. Under negative pressure, the cantilever is restored back to its original position covering the orifice, which reduces the opening size and increases valve resistance. For positive and negative driving pressures of equal magnitude, the reverse flow is always less than the forward flow.

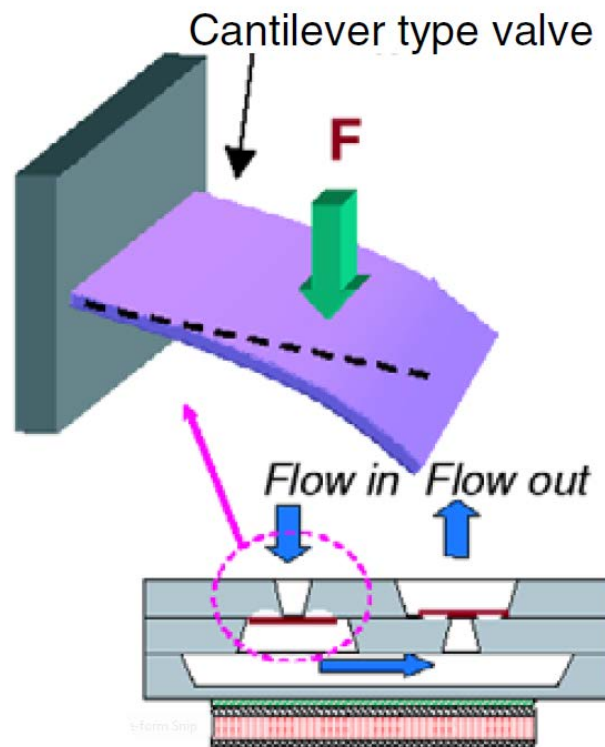


Figure 16. Cantilever-type valve operation [21]

By nature, the cantilever-type check valve is very versatile in design. By varying the thickness  $t$  or length  $a$  of the cantilever, or changing the location of the orifice relative to cantilever tip, large adjustments can be made to the pressure-flow characteristics. The orifice beneath the valve is the valve seat which the cantilever seals against in backflow, and its area

influences the force exerted on the flap. Because it affects the performance of the check valve, both parts, flap and orifice, must be developed in conjunction. Design considerations for the check valve include:

**-Diodicity:** A flexible cantilever is conducive to forward flow. In reverse flow, the orifice area is proportional to the sealing force on the cantilever. Leakage and backflow during the closing stroke must be minimized to achieve a high  $Di$ .

**-Resistance:** The hydrodynamic resistance of the cantilever is expected to be a major contributor to the overall system resistance. As always, resistance should be minimized.

**-Jet velocity:** The exit jet velocity should be maximized for imparting thrust. Once the hydrodynamic resistance of the flap valve is approximated, the orifice diameter can be optimized for jet velocity. The direction of the incoming and outgoing jets should be perpendicular, and is dependent upon valve positioning on the mantle.

For compliant flexure and reliable sealing, a soft material is desired. TangoPlus, the same material chosen for the gaskets, was selected as the cantilever flap material. Properties according to its manufacturer, Stratasys, are given in Table 7.

Table 7. TangoPlus FLX930 Properties

Tensile strength	1.15 MPa
Elongation at break	195%
Modulus of elasticity	0.6 MPa
Polymerized density	1.17 g/cm <sup>3</sup>

The flap valve was designed as a rectangular beam of length  $L = a + b$  from the base, width  $w$ , and thickness  $h$ . The pressure applied across the orifice area was modeled as a point load  $F$  applied at a distance  $a$  from the base. The deflection at the tip,  $\delta_L$ , and at position  $b$ ,  $\delta_B$ , were calculated, along with the area moment of inertia  $I$ .

$$\delta_L = \frac{Fa^3}{3EI} \left( 1 + \frac{3b}{2a} \right)$$

$$\delta_B = \frac{Fa^3}{3EI}$$

$$I = \frac{1}{12}wh^3$$

An initial, baseline valve design was formulated to have a forward flow resistance on the same order of the actuator resistance,  $R_{valve} \sim R_{act}$ . To estimate the resistance of the opened valve in forward flow, the gap between the flap and mantle was modeled as a rectangular window having cross-sectional width  $w$ , height  $\delta_B$ , and length  $d_{orifice}$ . The relation for resistance through a rectangular channel was used to calculate  $R_{valve}$ .

$$R_{valve} = \frac{12\mu d_{orifice}}{w\delta_B^3 \left( 1 - 0.630 \frac{\delta_B}{w} \right)}$$

The point force  $F$  can be approximated as

$$F = P_s A_{orifice} = (P_{max}) \left( \frac{\pi d_{orifice}^2}{4} \right)$$

Designing for  $\frac{R_{valve}}{R_{actuator}} \sim 1$ , a baseline cantilever was created with dimensions of  $L =$

$3 \text{ mm}$ ,  $w = 2 \text{ mm}$ ,  $h = 0.75 \text{ mm}$ , with orifice diameter  $d_{orifice} = 1 \text{ mm}$  located at  $b = 2 \text{ mm}$ .

This design served as a starting point for subsequent modifications.

For a constant cantilever aspect ratio  $\frac{h}{w}$ , the valve resistance scales as

$$R_{valve} \sim \left( \frac{Ewh^3}{d_{orifice}^2 L^3} \right)^4$$

Note that the cantilever thickness  $h$  and effective length  $L$  have a dominant influence on  $R_{valve}$ .

Once tests on the baseline valve were performed, slight adjustments to these dominating variables were made to improve the valve.

# **Chapter 5      Fabrication, Testing and Discussion**

Once the individual components were designed to fit together in a stacking architecture, they were fabricated predominantly using 3D-printing. A variety of methods were used to verify the proper functioning of each component. Based on initial component tests, some designs were fine-tuned before assembly. The fabrication, assembly, and testing procedures of the finalized design are discussed in this chapter.

## **5.1 Fabrication**

The individual components of the squid have been designed with fabrication simplicity in mind. The fabrication method for the most complex components, the mantle and check valve, featured 3D-printing technology. 3D-printing offers more design versatility and lighter materials than conventional machining, and is cheaper and faster than micromachining, which are all essential characteristics for rapid prototyping. Parts are built layer by layer from the bottom-up. Overhanging features are supported from underneath by removable support material, enabling the fabrication of many designs that would be impossible with machining.

There are many commercial 3D printers with varying levels of performance. The major distinguishers among 3D printers are printing method, materials selection, consistency, and print resolution. Size, cost, and speed are largely determined by the print resolution. For parts of the robotic squid, the Stratasys Connex 350 polyjet printer was used. The Connex has several unique features:

- prints with UV-curable photopolymer resins
- 16 micron Z-axis resolution
- multi-material printing with two resins simultaneously
- forms digital materials from two base resins
- compatible with a variety of rigid, flexible, and transparent materials

The two primary 3D-printed materials used to fabricate the squid are Tango Plus FLX980 and Vero White Plus RGD835. Tango Plus is a transparent soft, rubber-like material and Vero White Plus is a rigid plastic. Neither materials degrade in decane or NaCl, though slight swelling can occur.

Since the Connex printer is able to embed two materials into a single part, a soft gasket and valves were embedded in the mantle to create a monolithic part.

## **Gasket**

During gasket sealing tests, inconsistencies with printed soft materials were noticed. The Connex printer offers two material finishes: glossy and matte. The glossy finish can only be applied on the top-side of printed parts and those sides cannot be encased in support material. For gaskets not integrated with the mantle, the top side was printed glossy while the bottom was matte, shown in Figure 17.

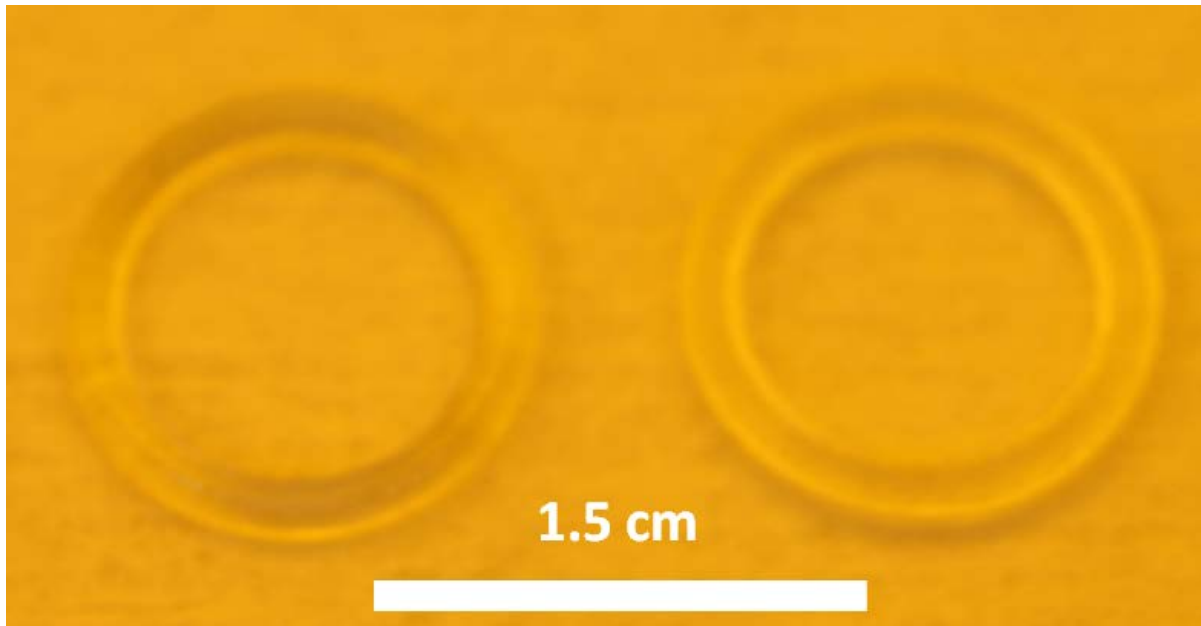


Figure 17. 013 O-ring Gasket, glossy side (left) and matte side (right)

Despite being of the same material, differences were noted in the two finishes. The glossy surface easily adheres to surfaces when compressed and is more reflective than matte. The matte side is not tacky and exhibited brittle behavior when heated to 120°C. Therefore, the glossy side was printed onto the mantles and compressed against the actuator plates.

### **Check Valves**

The check valves were first fabricated within valve test pieces for testing at constant pressures, without reciprocal pumping. The test pieces were printed from VeroWhite and the flap was printed from TangoBlackPlus, which is opaque but has identical properties as TangoPlus. A close-up of a test piece is shown in Figure 18.



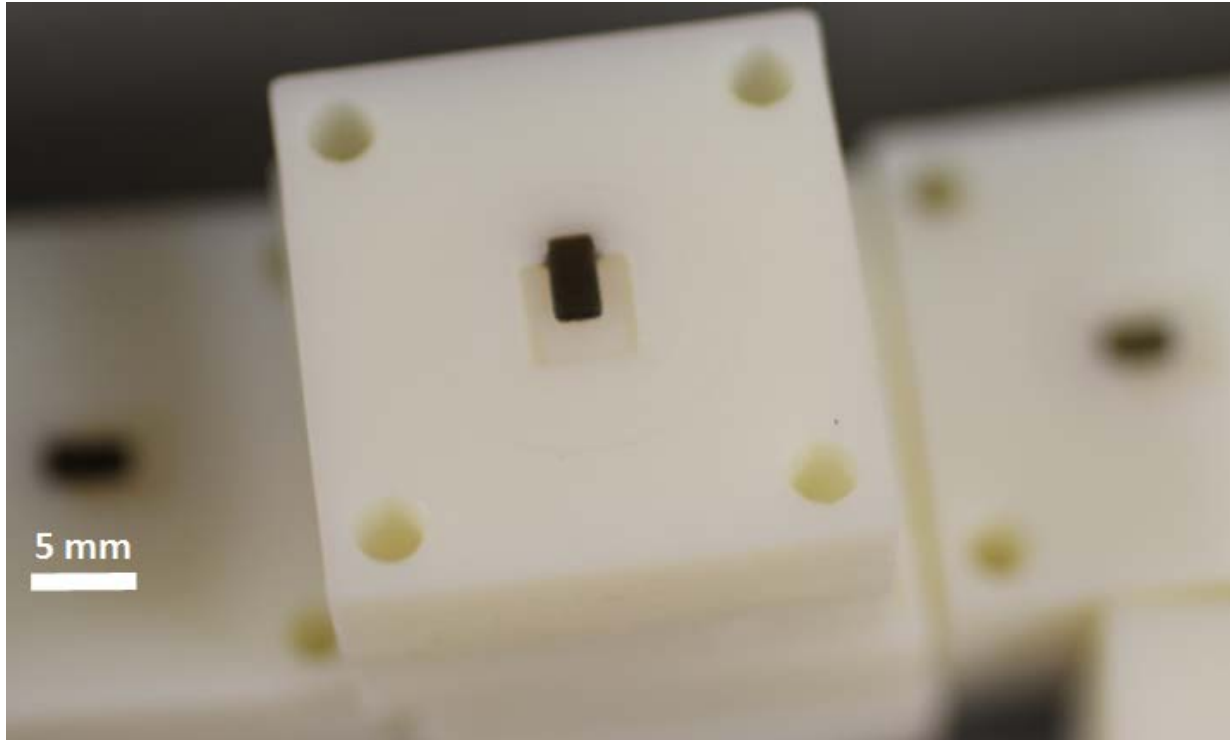


Figure 18. Valve test piece,  $3 \times 2 \times 0.75 \text{ mm}^3$  cantilever

When printed, the part is encased in support material which must be completely removed. The flap is attached to the supporting VeroWhite structure and must be released manually. This is done by peeling the flap from underneath with jeweler's screwdrivers, while taking care to not damage the valves. The printed flap in Figure 18 is longer than 3 mm, with the cantilever base enclosed on three sides by a valve fixture, which controls the length of flap peeled off. The excess length lies within this fixture and does not get released, so the effective cantilever length is 3 mm, in accordance with baseline design dimensions of  $L = 3 \text{ mm}$ ,  $w = 2 \text{ mm}$ ,  $h = 0.75 \text{ mm}$ , with orifice diameter  $d_{\text{orifice}} = 1 \text{ mm}$  located at  $b = 2 \text{ mm}$ .

## 5.2 Valve Testing

Static pressure tests were performed for a variety of cantilever dimensions. The valves were characterized with pressure plotted against conductance. The pressure displayed is the pressure drop across the valve portion of the system. Conductance is simply the inverse of hydrodynamic resistance. For each cantilever variation, the average diodicity from multiple valve tests are shown, starting with the baseline design in Figure 19 and Table 8.

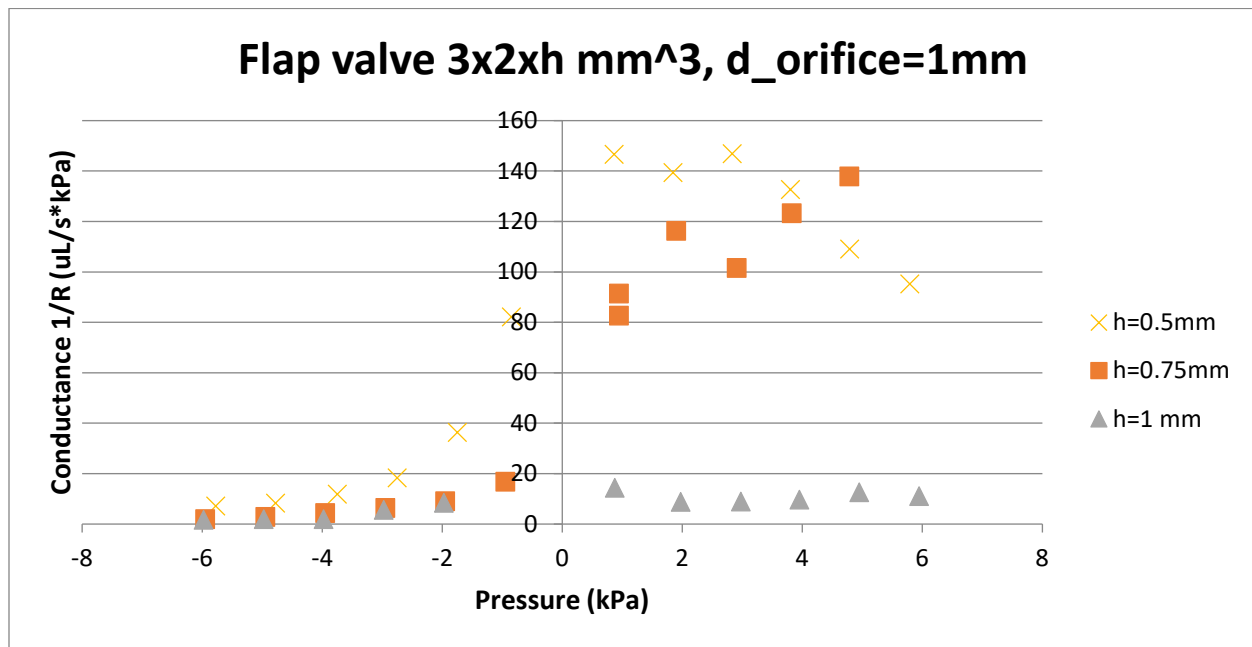


Figure 19. Flap valve performance

Table 8. Flap valve performance

Thickness (mm)	<i>Di</i>
0.5	8.41
0.75	14.97
1	3.00

The baseline design was first tested at different flap thicknesses. Thicknesses of 0.5, 0.75, and 1 mm were tested. Surprisingly, the thickness variation between 0.5 mm and 0.75 mm did not drastically affect the diodicity, according to the resistance scaling:

$$\frac{R_{valve1}}{R_{valve2}} \sim \left(\frac{h_1}{h_2}\right)^{12} = \left(\frac{0.75}{0.5}\right)^{12} = 130$$

Additionally, a non-monotonic trend is seen where the maximum diodicity is reported for 0.75 mm thickness. The thicker 1 mm flap has lower  $Di$  as expected, but the 0.5 mm thickness should in theory have a higher forward flow rate and higher  $Di$ . It is probable that the 0.5 mm flap will not properly seal against the orifice due to thermal stress within the cantilever flap incurred during printing.

Next, slight modifications were made to the cantilever, resulting in dimensions of  $3.25 \times 2.5 \times h \text{ mm}^3$ . The width was expanded, but the accompanying increase in length maintained  $\frac{R_{valve}}{R_{actuator}} \sim 1$ . The valve seat and flap were also redesigned to be curved with a radius of curvature of 4 mm. The results in Figure 20 and Table 9 show lower diodicities on average for the expanded flap. The curved 0.75 mm valve had a degraded  $Di$  when compared to the non-curved version, more so than the 0.5 mm valve, likely because the thicker valve does not properly conform over the curved orifice seat at the tested pressures.

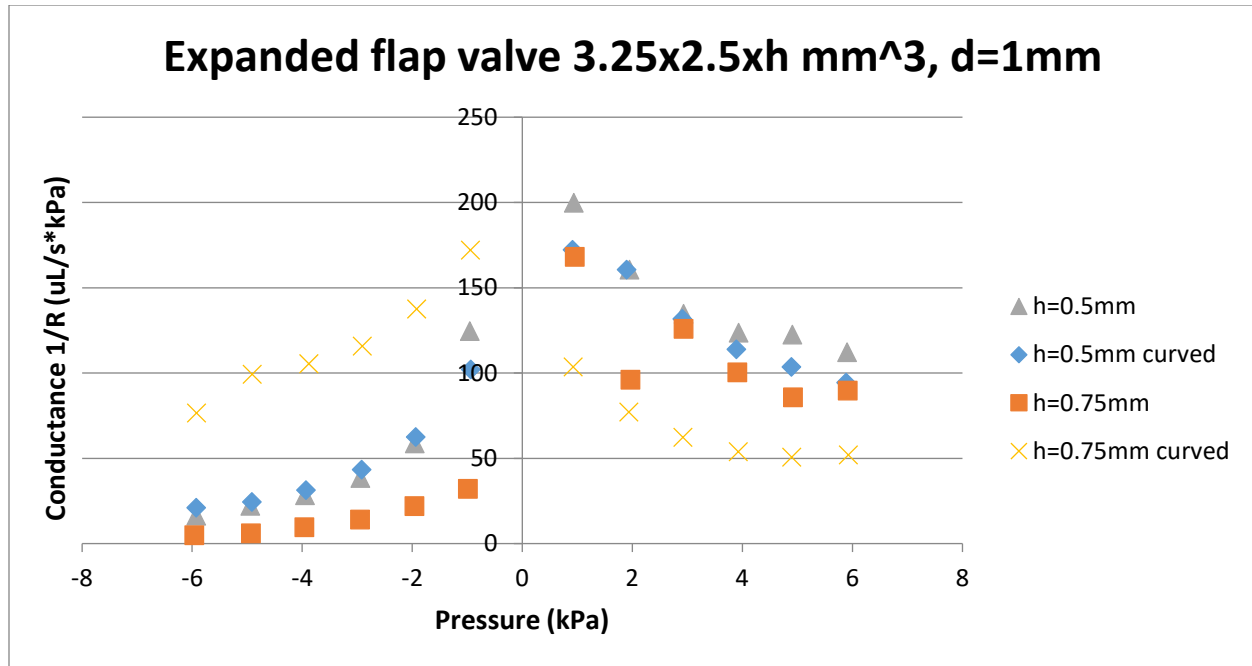


Figure 20. Expanded flap valve performance

Table 9. Expanded flap valve

Thickness (mm)	Curved	Di
0.5	N	4.02
0.5	Y	3.45
0.75	N	6.10
0.75	Y	0.82

The valve design was reduced to dimensions of 2 x 1.2 x 0.4 mm<sup>3</sup>, with a 0.3 mm orifice diameter. Again, these dimensions were balanced to offer a theoretical resistance on the order of  $R_{actuator}$ . This smaller design produced worse checking performance, with an average diodicity of 1.97.

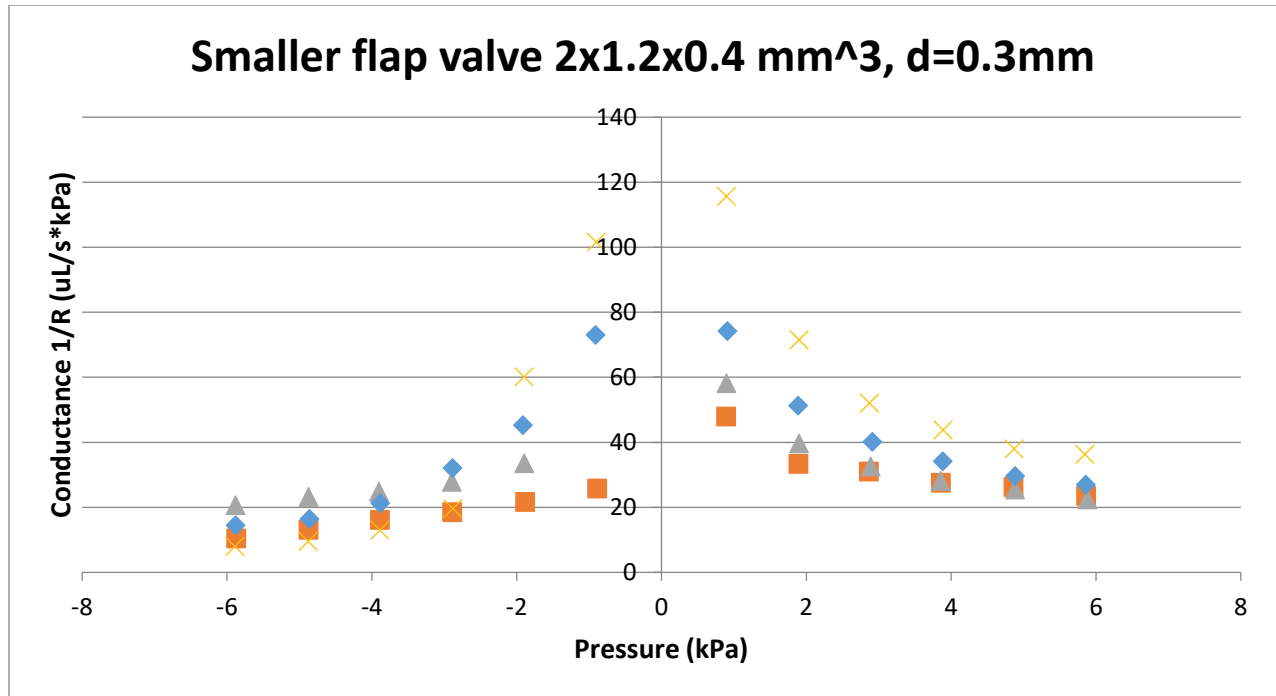


Figure 21. Smaller flap performance

The valve design was reduced to dimensions of  $2 \times 1.2 \times 0.4 \text{ mm}^3$ , with a 0.3 mm orifice diameter. Again, these dimensions were balanced to offer a theoretical resistance on the order of  $R_{actuator}$ . This smaller design worsened checking performance, with an average diodicity of 1.97.

Across these design variants, the original  $3 \times 2 \times 0.75 \text{ mm}^3$  flap exhibited the highest diodicity at 15. This valve, not including the orifice, has a hydrodynamic resistance about 15 times greater than the actuator itself ( $\frac{R_{valve}}{R_{act}} \sim 15$ ), showing the valve to be the dominant component of the squid circuit. To help with further design if needed, several general trends were noticed from analyzing the valve characterization results:

- No significant pressure was needed to initiate reverse flow through the valves, indicating a valve cracking pressure of  $P_{crack} = 0 \text{ kPa}$ .

-Diodicity is improved at larger pressure gradients, since the sealing force applied onto the flap in reverse flow is proportional to pressure.

-A smaller orifice in relation to flap size will decrease  $Di$  and cause results to deviate from the design approximation. This is due to the sealing force being proportional to the orifice area.

### **Micropumping**

The valve characterization results showed the  $3 \times 2 \times 0.75 \text{ mm}^3$  design to be superior. However, static pressure testing does not equate to pumping performance. The valve transition from its forward flow state to reverse flow state takes a finite time during which temporary backflow occurs. If the pumping actuator is pulsed at high enough frequencies, the valve will not be able to fully close. In this case the backflow is equal to the forward flow per actuation cycle, and the valve may not exhibit checking behavior at all. Thus, it is important to test the flap valves in micropumping to verify performance.

A pump test assembly resembling a diaphragm pump, like Figure 8, was used to pump decane. Figure 22 presents a schematic of the single-acting pump.

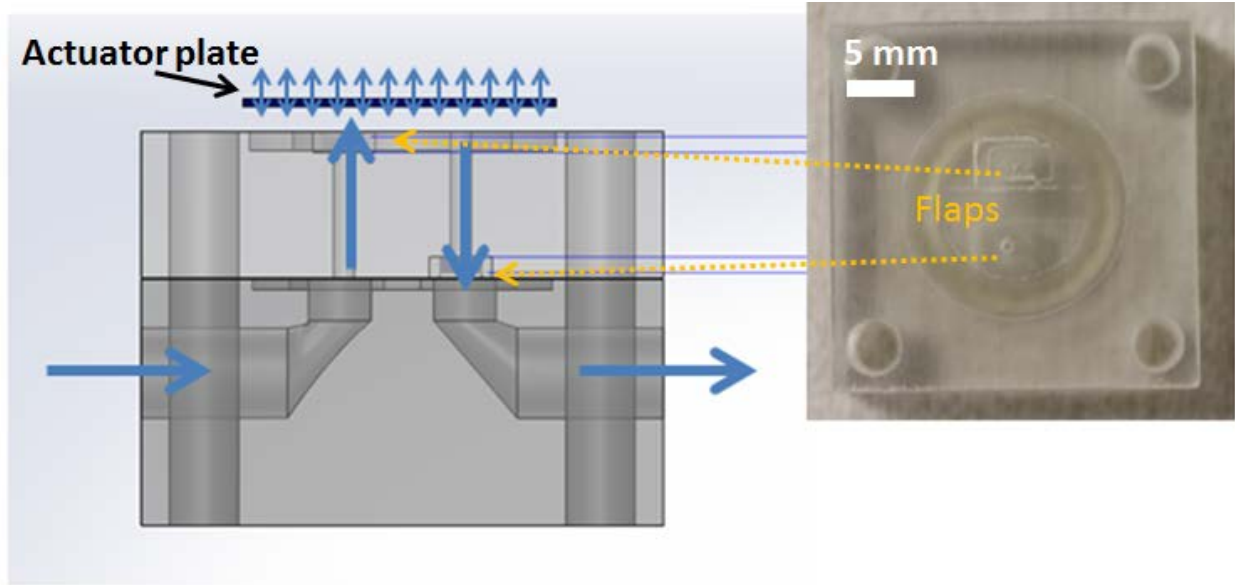


Figure 22. Pump test assembly design

Pumping was performed using 25  $\mu\text{m}$  D actuators under 4 kPa back pressure, about half the capillary pressure  $P_{max}$ . Keeping the same flap dimensions, different orifice sizes were used, up to 1 mm. Any larger orifice diameter would cause major reductions in the propulsive force, as estimated using the newly acquired  $R_{valve}$ .

Figure 23 shows the flowrate vs. frequency curves for the different orifice diameters. Interestingly, overall reverse flow is observed at frequencies under around 8 Hz. The reverse flowrates are attributed to inertial effects at low pressure drops across the valves. At around 20 Hz, the pumps with 1 mm diameter orifices reach a local peak flow rate. A best volumetric flow rate of 1787  $\mu\text{L}/\text{min}$  is achieved at 18 Hz actuation frequency. Further increases in frequency showed negligible flowrates, unmarked on the plot, with the exception at 40 Hz due to resonant effects. At some frequencies a backflow issue was encountered where there was zero net flow because the backflow during the valve closing stroke was equal to the forward flow. However,

no clear correlation was found between the net flowrate and backflow, although an inverse trend was expected because of larger pressure differentials across the valve at higher  $Q$ .

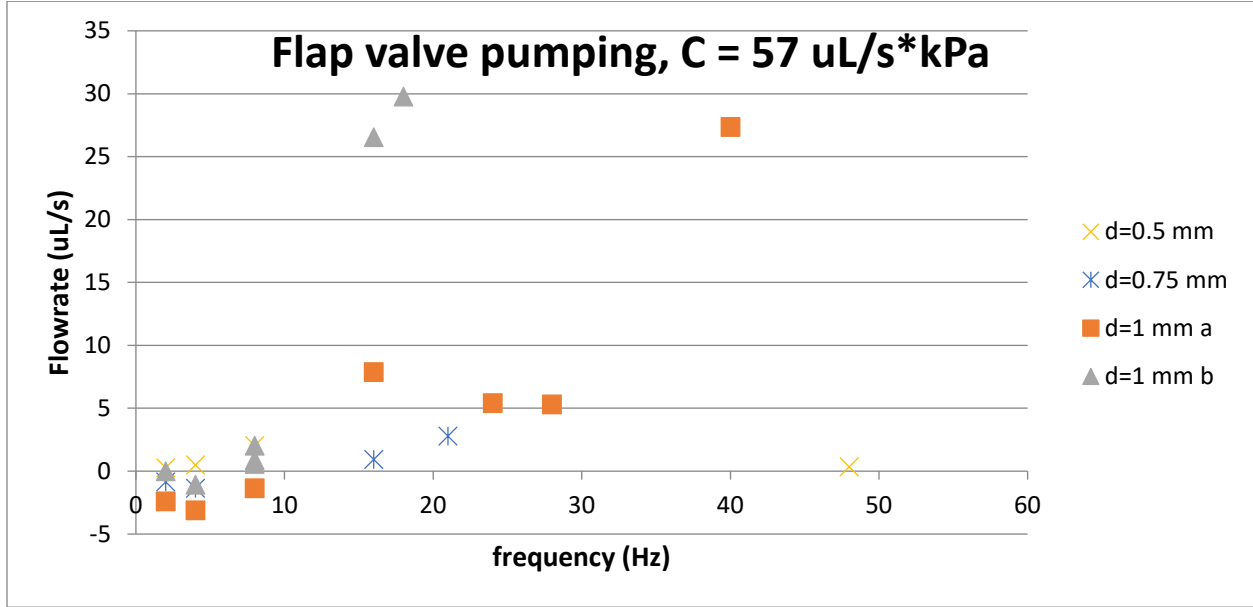


Figure 23. Pumping using designed flap valves

The theoretical flowrate and pumping power are calculated as:

$$Q_{theory} = V_{displacement} f_{actuation}$$

$$\dot{W}_{pumping} = Q_{forward}^2 R_s$$

with actuation frequency  $f_{actuation}$ , forward flow rate  $Q_{forward}$ , system hydrodynamic resistance  $R_s$ . In comparison to the theoretical values, the micropump produces 33% of the theoretical flowrate and operates at 10.8% power efficiency. The large discrepancy is confirmation that valve diodicity in static pressure conditions does not directly translate to pump performance.

As mentioned for static pressure testing, the orifice diameter affects diodicity. For pumping applications, this creates a tradeoff between diodicity and backflow as the orifice



diameter is changed. Increasing orifice area will increase the sealing pressure under a negative pressure differential, but the backflow volume through the larger orifice during valve closing is increased. For larger displacement-to-backflow ratios,  $V_{displace} \gg V_{backflow}$ , the problem diminishes as long as there is negligible leakage through the check valve. Conversely, an orifice that is too small will not be able to exert enough sealing force on the flap to completely seal the valve. This increases leakage as was seen in static testing, but it also increases the time for valve closing, during which more backflow is allowed through the orifice.

Throughout the pumping experiments, valve consistency frequently presented a concern, as was apparent by observing variations among similar flap valves. At some actuation frequencies, markedly different flow rates were observed for the same frequency. This is indicative of the limited reliability of 3D-printing at small dimensions. It has been noticed that properties and accuracy of printed parts can be highly inconsistent at feature sizes below 0.1 mm. Plausible reasons for inconsistencies are over-curing, surface roughness, and swelling. This poses a fabrication technology-based limitation which should be mitigated as printer resolution continues to improve.

## 5.3 Assembly

The squid assembly procedure consists of the following major steps: 1) stacking, 2) compression, 3) buoy attachment, 4) electrical connection, 5) decane immersion, 6) air purge, 7) NaCl injection. Detailed steps are given in the assembly procedure:

1. Clean and prepare components. Insert gauge 32 biopsy tool into O-ring. Eject core.
2. Align and stack components, with biopsy tool directed toward the front.

3. Fit 1 cm segment of heat shrink tubing around assembly, then compress under clamp.
4. Apply heat using heat gun until tubing has conformed to the shape of the assembly (Figure 24).
5. Cut openings through tubing to expose inlet orifices.
6. Cut out 1.9 cm<sup>3</sup> polystyrene block and tape onto side of assembly with double-sided polyimide tape. Do not block the inlet orifices.
7. Connect lead wires to actuators and electrode plate by inserting O-ring slices (Figure 25).
8. Place assembly onto dock above decane tank and clip voltage connections onto leads.
9. Slowly immerse assembly in decane tank. The squid assembly should float (Figure 26).
10. Connect decane-filled syringe to biopsy tool and apply negative pressure to extract air from within.
11. Remove decane syringe and attach NaCl syringe. Inject NaCl under 8 kPa. Wait for 3 minutes to detect leaks. If there are no leaks, proceed to next step.
12. Slowly remove biopsy tool from gasket.

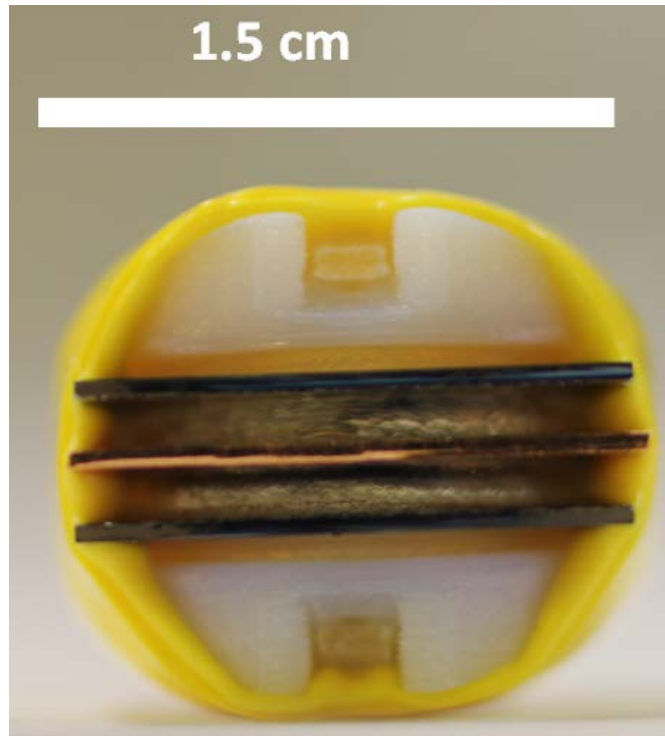


Figure 24. After step 4

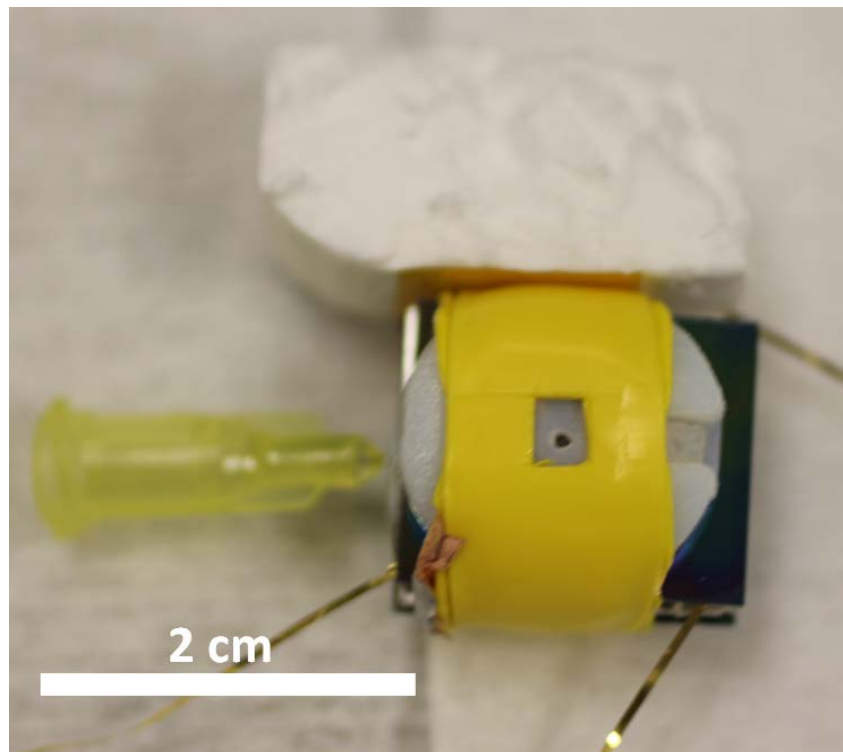


Figure 25. After step 7

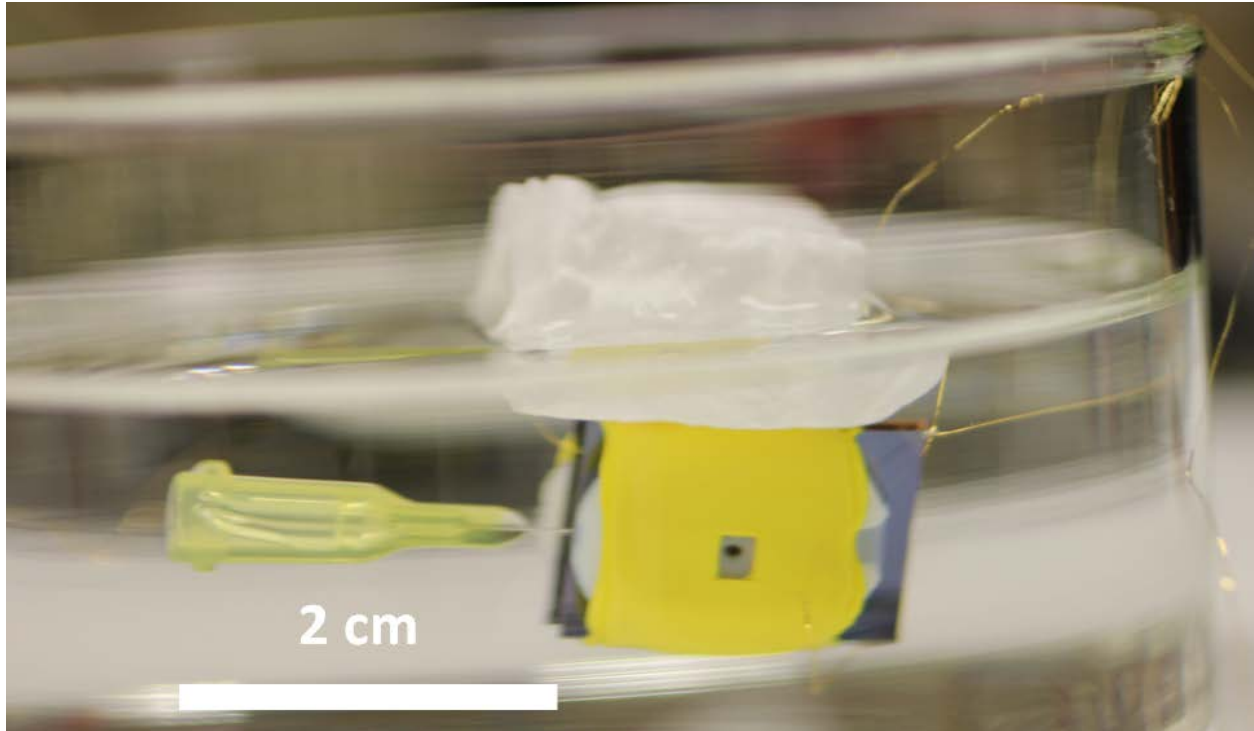


Figure 26. After step 9

## 5.4 Discussion

After the robotic squid has been assembled and filled with the appropriate liquids, testing can then be performed. The relevant system metrics to be acquired are velocity, thrust, efficiency, and reliability. From the momentum flux-based modeling, the predicted swimming velocity is 3.0 cm/s under a continuous thrust of  $F_{thrust} = 87 \mu N$ . Although this velocity has not been achieved yet, there are several factors that can account for a reduction in swimming speed.

- Air bubbles:** Electrolysis-produced bubbles interfere with the transfer of back pressure between the actuators

- Oxide clogging:** Electrolysis-produced metal oxides can clog the capillaries and reduce displacement volume

**-Jet orientation:** The entering and exiting jets are not completely perpendicular. If the exiting jet is not concentrated, the momentum can diffuse outward away from the movement axis.

**-Vortex ring formation:** Despite a small orifice, the assumption of a fluid plug entering and exiting the squid may not be entirely accurate. Vortex rings formed at the orifices can alter the direction from which fluid flows into and out of the valves, which in turn affects net momentum transfer. The influence of vortex rings can be simulated and visualized using digital particle image velocimetry.

Although the proposed robotic squid design utilizes microhydraulic electrowetting actuators, in theory any type of micro actuator that can be used in diaphragm pumping can be adapted to drive propulsion.

# Chapter 6      Conclusions

## 6.1 Summary

A bioinspired, mini-robotic squid platform has been designed. The microhydraulic electrowetting actuator is integrated as the driving component, which offers several advantages over existing microrobotic platforms by offering efficient and reliable actuation at low-voltages. High power density scaling is derived and proven at different capillary diameters. The MEA has the potential to advance the state of the art in enabling remotely operable systems, where an external power source is not required for the ability to operate for long periods of time. The squid is propelled by the impulse imparted from a continuous momentum flux, and is described by a simplified control volume analysis and transient flow rate model.

The current design incorporates double-acting actuators excited by electrical waveforms in quadrature. This double-acting diaphragm pump arrangement has the advantages of higher driving pressures without the need of a deformable membrane. A stacked architecture is built around the actuators to form a symmetric device consisting of the electrode ring, mantle pieces, and check valves. A cantilever-type flap check valve is chosen to maintain unidirectional flow. After several variants are tested, the most promising designs are tested in the context of micropumping, which is shown to be necessary as measured flow rates can greatly depart from theoretical flow rates. Assembly procedures for the robotic are listed, followed by a discussion of testing directions for the squid.

## 6.2 Future Work

Apart from optimization of the components already discussed, the initial design of a mini-robotic squid leaves much room for improvement. There are still many important features to be addressed and added, such as:

- Untethered operation**

- Directional steering:** The ability to control the direction of thrust will allow for greater maneuverability.

- Depth control:** Electrolysis-induced bubbles can be exploited for buoyancy adjustment. This has previously been demonstrated in an underwater biped robot made by [22], where electrolysis-generated bubbles adsorbed to the actuator to increase buoyancy.

- Energy harvesting:** An aquatic swimming environment presents many sources for energy harvesting (solar, tidal, wave).

- Dimensional accuracy:** As additive manufacturing methods continue to expand and improve, the capability to directly print materials such as metals and dielectrics will open up vast design opportunities with more accurate tolerances. For the squid design, such advances could allow for fully automated fabrication.

The field of microrobotics is ripe for innovation. For constantly decreasing size, weight, and power requirements, robotic devices at the centimeter scale and below can be deployed for many diverse applications, to include surgery, surveillance, and environmental monitoring. Budding manufacturing technologies like 3D-printing are slated to enable robotics fabrication at ever smaller scales. Though such a reality is far off given the current pace of microrobotics

research, it is hoped that the mini-robotic squid design introduced herein will help catalyze interest in microrobotics research and collaboration.



# Bibliography

- [1] J. Kedzierski, K. Meng, T. Thorsen, R. Cabrera and S. Berry, "Microhydraulic Electrowetting Actuators," *Journal of Microelectromechanical Systems*, vol. 25, no. 2, 2016.
- [2] M. Krieg and K. Mohseni, "Dynamic Modeling and Control of Biologically Inspired Vortex Ring Thrusters for Underwater Robot Locomotion," *IEEE Transactions on Robotics*, vol. 26, no. 3, pp. 542-554, 2010.
- [3] A. P. Thomas, "Exploration into the feasibility of underwater synthetic jet propulsion," California Institute of Technology, 2007.
- [4] M. Rubenstein, C. Ahler and R. Nagpal, "Kilobot: A Low Cost Scalable Robot System for Collective Behaviors," in *IEEE International Conference on Robotics and Automation*, Saint Paul, Minnesota, USA, 2012.
- [5] M. Sitti, H. Ceylan, W. Hu, J. Giltinan, M. Turan, S. Yim and E. Diller, "Biomedical Applications of Untethered Mobile Milli/Microrobots," *Proceedings of the IEEE*, vol. 103, no. 2, 2015.
- [6] M. Read, C. Moslinger, T. Dipper, D. Kengyel, J. Hilder, R. Thenius, A. Tyrrell, J. Timmis and T. Schmickl, "Profiling Underwater Swarm Robotic Shoaling Performance using Simulation," CoCoRo Project, 2011.
- [7] M. Karpelson, G.-Y. Wei and R. J. Wood, "Milligram-Scale High-Voltage Power Electronics for Piezoelectric Microrobots," in *International Conference on Robotics and Automation (ICRA)*, 2009.
- [8] R. S. Fearing, "Powering 3 Dimensional Microrobots: Power Density Limitations," *1998 Tutorial on Micro Mechatronics and Micro Robotics*, 27 September 1998.

- [9] Y. Fu, J. Luo, A. Flewitt, W. Huang, S. Zhang, H. Du and W. Milne, "Thin film shape memory alloys and microactuators," *Int. J. Computational Materials Science and Surface Engineering*, vol. 2, 2009.
- [10] J. E. Huber, N. A. Fleck and M. F. Ashby, "The selection of mechanical actuators based on performance indices," *Proceedings of the Royal Society A*, vol. 453, no. 1965, 1997.
- [11] M. Karpelson, G.-Y. Wei and R. J. Wood, "A Review of Actuation and Power Electronics Options for Flapping-Wing Robotic Insects," in *IEEE International Conference on Robotics and Automation*, Pasadena, CA, 2008.
- [12] M. Sadeghi, H. Kim and K. Najafi, "Electrostatically driven micro-hydraulic actuator arrays," in *2010 IEEE 23rd International Conference on Micro Electro Mechanical Systems (MEMS)*, Wanchai, Hong Kong, 2010.
- [13] M. D. Volder and D. Reynaerts, "Pneumatic and hydraulic microactuators: a review," *Journal of Micromechanics and Microengineering*, vol. 20, 2010.
- [14] F. Mugele and J.-C. Baret, "Electrowetting: from basics to applications," *J. Phys: Condens. Matter*, vol. 17, pp. R705-R774, 2005.
- [15] S. M. Disney and R. D. Warburton, "On the Lambert W function: Economic Order Quantity applications and pedagogical considerations," *International Journal of Production Economics*, vol. 40, no. 2, pp. 756-764, 2011.
- [16] B. Koo and C.-J. Kim, "Evaluation of repeated electrowetting on three different fluoropolymer top coatings," *Journal of Micromechanics and Microengineering*, vol. 23, no. 6, 2013.
- [17] I. K. Bartol, P. S. Krueger, J. T. Thompson and W. J. Stewart, "Swimming dynamics and propulsive efficiency of squids throughout ontogeny," *Integr. Comp. Biol.*, vol. 48, no. 6, pp. 720-733, 2008.

- [18] D. J. Staaf, "Aperture effects in squid jet propulsion," *Journal of Experimental Biology*, vol. 217, pp. 1588-1600, 2014.
- [19] A. Glezer and M. Amitay, "Synthetic Jets," *Annual Review of Fluid Mechanics*, vol. 34, pp. 503-529, 2002.
- [20] Z. Travnicek, V. Tesar and J. Kordik, "Performance of synthetic jet actuators based on hybrid and double-acting principles," *Journal of Visualization*, vol. 11, no. 3, pp. 221-229, 2008.
- [21] K. W. Oh and C. H. Ahn, "A review of microvalves," *Journal of Micromechanics and Microengineering*, vol. 16, no. 5, 2006.
- [22] S. Guo, Y. Okuda and K. Asaka, "Hybrid type of underwater micro biped robot with walking and swimming motions," in *Mechatronics and Automation, 2005 IEEE International Conference*, Niagara Falls, Ont., 2005.